University of Nairobi

Institute of Nuclear Science and Technology

Local structure of proton conducting

Y-doped $AZrO_3$ (A=Ba, Sr, Ca) perovskites

CAROLINE WANJIRU MBURU

S56/65120/2010

A Thesis submitted for the partial fulfilment for the degree of Master of Science in Nuclear Science in the Institute of Nuclear Science & Technology in the University of Nairobi

Declaration

This thesis is my original work and has not been presented for a degree in any other university.

Signature ..... Date .....

Mburu, Caroline Wanjiru (S56/65120/2010)

This thesis has been submitted for examination with our knowledge as University supervisors

Professor Michael J. Gatari (PhD) Sign .....

Institute of Nuclear Science & Technology

College of Architecture and Engineering Date .....

University of Nairobi

Professor Maths Karlsson (PhD) Sign .....

Department of Applied Physics

Chalmers University of Technology Date .....

SE-412 96 Gothenburg S

Abstract

Burning of fossil fuels has disastrous implications on the environment due to emissions of nitrogen oxides, sulphur oxides and a wide range of toxic organic and inorganic compounds. We are also about to deplete the available natural energy sources and therefore research to find new, sustainable and clean energy sources are crucial for the benefit of present and future generations. Hydrogen fuel cells provide one such alternative and therefore research and development of fuel cells (Fuel cells, 2011) is important. The cells convert chemical energy directly into electrical energy and have an advantage over conventional means of power generation due to their high-energy conversion efficiency besides being environmentally friendly. The first fuel cell was demonstrated over 160 years ago but development continued inhibited by lack of attractive materials, which have high conductivity in the intermediate temperature region of 200 to 500 ˚C.

This thesis is based on experimental studies carried out on perovskite structured yttrium doped barium zirconate, calcium zirconate and strontium zirconate systems. The main work included synthesis of yttrium doped barium zirconate with different Y concentrations, followed by studying the local structure of the system as a function of Y concentration and the influence of protons on the local structure surrounding the Y ions. The experiments were performed using x-ray powder diffraction (XRD), to study the average structure of the perovskite lattice, and infrared (IR) and luminescence spectroscopy to study the local structure of the material.

The results indicated that increasing Y concentration leads to a slight, but clear, distortion of the local structure of the perovskite and we also found a dependence on hydration. Moreover, the results showed the symmetry around the Y atom was more distorted in the dry sample than in the hydrated. For the 20% Y doped $BaZrO_3$ sample in particular, spectral differences could not be resolved with the techniques used, which would motivate a further study of the local ordering of the dopant atoms

Acknowledgments

I set out on a journey.... It was a long Journey and it is coming to a close... To this far I have gotten; I would like to acknowledge the International Science Program (ISP) and the University of Nairobi for the financial support throughout project.

The KMF Group, for being very welcoming and making my working environment very conducive with Special thanks to *Ezio* for fixing for me the instruments all the time. It made my work easier and *Dharshi* you were far too kind.

The Oxide Group... in particular *Francis* and *Habibur* Thank you for guiding me through the chemistry lab work. Thanks to the entire chemistry department.

My supervisors, *Maths* I deeply appreciate all the guidance throughout the project... from when I was clueless to the point where I can confidently use Latex to prepare my final report... *Chris* for giving a nice welcome to the oxide group and teaching me the synthesis and the healthy project discussions throughout the project and *Michael Gatari* for the guidance and encouragement and even introducing me to academia and research.

Family and Friends... by believing in me, being by my side... I am forever indebted to you... My journey would have been incomplete without you.

The God given talents, patience, will perseverance and ability to motivate self at the difficult times, adaptation to the different and beautiful city of Gothenburg, for this I thank God.

Contents

List of Figures

Equations

$H_2O+V_o^{\cdot\cdot}+O_o^x \Leftrightarrow 2O\text{-}H_o^{\cdot}$ 2.1

$n\lambda = 2dsin\theta$ 2.2

$A = -\log_{10} T$ 2.3

List of abbreviations

XRD	X-ray diffraction
SOFC	Solid oxide fuel cell
IR	Infrared
TGA	Thermo gravimetric analysis
ICDD	International Centre for Diffraction Data
FTIR	Fourier transforms infrared
NIR	Near infrared
MIR	Mid infrared

Chapter 1

Introduction

1.1 Background

Energy is essential for our everyday lives. It is needed for basic food preparation to running industries and we therefore need a reliable source of energy. Global energy systems are changing for example oil and gas exploration and production in some countries for example recently found oil wells in Turkana area in Kenya, retreat from nuclear electricity dependence in some countries (Germany has planned shutdown of its nuclear power plants) and increasing policy focus on energy efficiency (IEA, 2012). Africa accounts for a meagre 5.8% of the world energy consumption according to the world energy statistics (WES, 2012). From the World Bank report on energy (WB, 2012), 1.3 billion people do not have access to electricity worldwide and 550 million of them are in Africa. It is projected that by the year 2030, 90-100 million people in sub-Sahara Africa will be without electricity. This means the poor will be deprived of the most basic human rights and economic opportunities to improve their standards of living.

Kenya is committed to becoming a globally competitive and prosperous country through implementation of a long-term strategic plan, Kenya Vision 2030 (KV30, 2010). A key important area in achieving the vision is boosting Kenya's production capacity and this implies higher energy requirements to sustain the envisioned economy. The country wants to boost its energy production capacity to 17 GW to enable it sustain economic development and to export any surplus to the neighbouring countries. About 70% of electricity supply is from hydropower generation whose sustainability and efficiency is threatened by frequent draughts, drying wetlands and receding underground water. The heavy reliance on wood fuel and kerosene for energy and lighting by a large population, production of over 20% of electricity from fossil fuel coupled with extra demand to support accelerated and sustainable economic development is environmentally unfriendly and calls for

alternative sources of energy and fuels (NEP, 2004). Burning of fossil fuels has disastrous implications on the environment due to emissions of nitrogen oxides, sulphur oxides and a wide range of toxic organic and inorganic compounds. We are also about to deplete the available natural sources and thus research and development of alternative sources of energy especially fuel cells (Fuel cells, 2011) is crucial for the benefit of present and future generations in Kenya. It is therefore necessary to find new, sustainable and clean energy sources and hydrogen fuel cells provide one such alternative.

A fuel cell converts chemical energy directly into electrical energy. It consists of an anode (negative side), a cathode (positive side) and an electrolyte for the energy-producing device. Electrons are drawn from the anode to the cathode through an external circuit producing direct current. Oxygen enters the fuel cell at the cathode; it combines with electrons flowing from the electrical circuit and hydrogen ions (protons) that have moved through the electrolyte from the anode to cathode. Together, the hydrogen and oxygen ions form water which drains from the cell. The protons and electrons are the product of hydrogen dissociation on interaction with the anode catalyst (Fuel cells, 2012; Ormerod, 2002)

Fuel cells are advantageous over conventional power generation due to their high efficiency in chemical energy conversion into electrical energy. The conversion process involves diminished emissions of nitrogen oxides (NOx), sulphur oxides (SOx) and hydrocarbons (HC) depending on the fuel used (FTD, 2011). They also have significantly reduced carbon monoxide emissions, which have adverse implications in human health, ecosystems and climate change thus making fuel cells environmental friendly. The fuel cells have applications in combined heat and power systems, in the range of 1-100 KW, in small scale and remote standalone applications (Ormerod, 2002). They are also important for applications where there is a requirement for high quality uninterrupted powers supplies that are eventually developed into large scale power generation.

1.2 Problem statement

Despite all the advantages, commercialization of fuel cells has been delayed due to the performance of their component materials. In particular, it has been difficult to develop fuel cells for the intermediate temperature range (200-500 ˚C) as seen in figure 1.1 (Norby, 1999). This is unfortunate because operating a fuel cell below 500 ˚C is a sufficiently low temperature to allow the use of relatively affordable materials and components, while 200 ˚C is high enough to give a wide flexibility in fuel and reduce the amount of expensive noble catalysts on the electrodes. At below 200 ˚C, there is fuel refinement and therefore the temperature range is not ideal. The main difficulty that has hindered the development of such fuel cells has been to find electrolytes with sufficiently high proton conductivities. However, proton conducting perovskite type oxides have emerged as a promising class of materials for this purpose. Norby (2001) reported that all known electrolytes have flaws; consequently concerted efforts in searching for acceptable electrolytic materials are necessary.

1.3 Justification

Proton conducting perovskites were initially investigated by Iwahara et al. (1981), and they have indeed been successfully used as electrolytes for numerous applications in fuel cells, sensors and batteries. Solid oxide ceramics have been the subject of rigorous research due to their inherent advantages as electrolytes. They have high efficiency compared to combustion-based technologies, low emissions and fuel flexibility (Malavasi et al., 2010). Many successful low temperature proton conductors, below 100 ˚C are polymer based. Nafion® is the most studied one, with a conductivity of the order 10^{-1} S cm^{-1} about 90 ˚C (Norby, 1999). In the 100–200 ˚C range, several inorganic acid compounds (solid acids), e.g. $CsHSO_4$ and $Rb_3H(SeO_4)_2$, exhibit a phase transition to a ”superprotonic” state where the conductivity jumps by several orders of magnitude to a value of 10^{-1} to 10^{-3} S cm^{-1} (Kreuer, 2002).

In the high temperature range, above 600 ˚C, many hydrated perovskites show high proton conduction (Norby, 1999). One of the best is Y-doped $BaCeO_3$, which reaches a maximum conductivity of ~10^{-2} S cm^{-1} at about 600 ˚C (Norby, 1999). In the intermediate temperature range 200–500 ˚C, a 'gap' characterizes the lack of available materials possessing high proton conduction (here about 10^{-2} S cm^{-1} and higher (Figure 1.1). Proton conductors at intermediate temperatures would also be attractive in many applications. It is therefore of high interest to find materials that can close the gap.

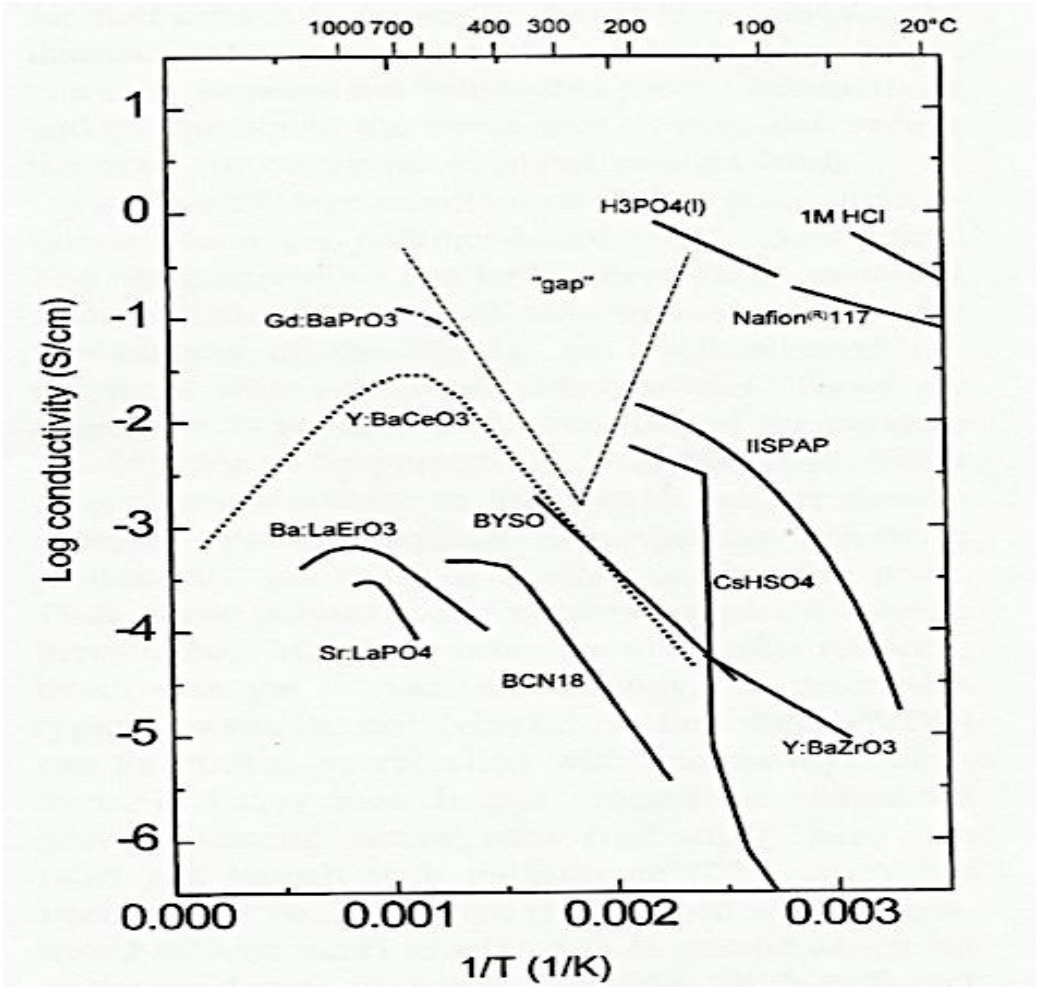

Figure 1.1: Arrhenius plot of state of the art conductivities over a large range (20 - 1000 ˚C). Adapted from Norby (1999).

Several hydrated perovskites show high proton conductivity at the upper limit of the intermediate temperature range (Kreuer, 2003), and it is anticipated that some of these can be modified and made high proton conducting at lower temperatures. Therefore, further research on these materials may develop new solid proton conductors for applications in the intermediate temperature range (Norby, 1999). This work was therefore planned to understand proton-conducting perovskites with a specific interest of investigating the characteristics of yttrium doped $AZrO_3$ (A= Ba, Sr or Ca) perovskites.

1.4 Objectives

The main objective was to investigate proton conduction characteristics at varied levels of doping barium zirconate perovskites with yttrium at intermediate temperatures and to extend the investigation to strontium zirconate and calcium zirconate with 2.5% yttrium doping. The specific objectives were to:

1. Synthesize barium zirconate with different yttrium doping concentrations, and calcium zirconate and strontium zirconate at 2.5% yttrium doping.
2. Study the local structure of yttrium doped $BaZrO_3$ as a function of yttrium concentration.
3. Study the local structure of $AZrO_3$ as a function of A site cation. (A= Ba, Sr or Ca).
4. Investigate the influence of hydration on the local structure of the above mentioned materials.

Chapter 2

Literature Review

2.1 Introduction

There have been numerous studies done on different aspects of proton conducting perovskites. These studies involve synthesis, vibrational spectroscopy and atomic simulations. The most commonly used electrolyte is the yttrium-stabilized zirconia (YSZ). This is a fluorite-structured oxide (AO_2 A= Zr). The YSZ exhibits good conductivity at temperatures 800–1000 $^{\circ}$C. This high working temperature makes it problematic for use in small-scale applications. Thus new materials with a lower operating temperature need to be developed (Malavasi et al., 2010)

2.2 Survey of study field

Iwahara et al. (1990) studied Y doped $SrZrO_3$ and found that protons are bound in the interstitial sites between the oxygen ions and migrate by thermal activation process. Infrared absorption measurements of $SrZrO_3$ crystals show two broad bands around 2400 cm^{-1} and 3200 cm^{-1}, which is characteristic of O-H stretching vibrations. The free O-H stretch is observed at 3500 cm^{-1}. This can be associated with protons in the perovskite structure. At 5% yttrium doping, activation energy of 0.45eV was obtained.

D'epifano et al. (2007) described synthesis of ABO_3 (A= Ba, Ca or Sr; B= Zr) perovskite through citric acid based sol-gel with water and ethylene glycol as the solvent. The technique was used to synthesise single-phase 20% yttrium doped barium zirconate ($BaZrO_3$) powders. More powders of different doping levels were also synthesised and calcined at 1100 $^{\circ}$C from which XRD patterns showed pure perovskite structure (Fabbri et al., 2010). Single-phase crystals were obtained up to 50% level of yttrium doping. The samples were hydrated to add protons in the material and the level of proton uptake was determined using thermal gravimetric

analysis (TGA) and the proton uptake was observed to increase with increasing level of doping. Interestingly, the larger proton concentration did not result in proton conductivity enhancement but rather reduced. The reduced conductivity was attributed to the structural distortion inferred by Y-doping and possibly trapping of protons at the Y sites.

In another study by Yajima et al. (1991), yttrium doped $SrZrO_3$ showed appreciable proton conduction in proton and hydrogen-containing atmospheres. In a hydrogen atmosphere, the oxides became almost pure proton conductors although they showed proton and mixed conduction in a water vapour atmosphere. Other proton conducting perovskites have been studied to find the stable electrolyte with higher proton conductivity.

Only electrolytes based on high Y doped $BaZrO_3$ combined high bulk proton conductivity with high stability in a unique way. Aliovalent dopants with matching ionic radii to the B site atom are traditionally chosen for oxide ion conductors. Sc doped zirconia ion conductors show higher oxide ion conductivity than Y doped zirconia. However, for proton conductivity, Y doped zirconia shows higher proton conductivity than Sc or In doped zirconia. In Y doped zirconia, proton mobility and activation enthalpy is independent of the dopant concentration. Y on the Zr site usually expands the lattice locally and leads to tetragonal distortions at concentrations above 5%, although it leaves the acid/base properties of the coordinating oxygen almost unchanged (Kreuer, 2003).

Using different trivalent acceptor dopants on $BaZrO_3$ B site, Karlsson et al. (2010) showed that the acceptor doping leads to local structure distortions of the average cubic structure. It was however noted that the effect of doping was stronger in the Raman than in the IR spectra. The Raman spectrum of the doped material is different from that of the undoped $BaZrO_3$.

In a study of the vibrational properties of protons in the hydrated perovskite system $BaIn_xZr_{1-x}O_{3-\delta}$ for different dopant concentrations using Infrared and Raman

spectroscopy by Karlsson et al. (2005), doping with In on the B site was observed to lead to significant local distortions of the average cubic structure. The local distortions became more pronounced with increasing dopant concentrations, however they had no correlation to the oxygen vacancies.

Omata et al (2004) in their study of infrared diffuse reflection spectra of the O-H stretching vibration region was used to characterize proton dissolution sites in High Temperature Proton Conductors of $CaZrO_3$, $SrZrO_3$ and $BaZrO_3$ doped with trivalent Ga^{3+} In^{3+} and Y^{3+} ions. For $CaZrO_3$, the diffraction peaks corresponded to orthorhombic perovskite-related phase and the determined lattice parameters were consistent with the presence of the dopant. The IR spectra for the 5% Y^{3+} doped sample, a sharp band was observed for the sample annealed in water vapour. For the 5% Y doped $SrZrO_3$ annealed in water vapour atmosphere a broad absorption spectrum from 3700 to 1700 cm^{-1} was observed. There were five bands, 3327, 3043, 2498, 1897, 1747 cm^{-1} . The five O-H bands observed correspond to five different proton dissolution sites in $SrZr_{0.95}Y_{0.05}O_{3-\delta.}$ $BaZr_{0.95}Y_{0.05}O_{3-\delta}$ annealed in water atmosphere consisted of two ν_{OH} bands corresponding to proton dissolution sites at 3465 and 3309 cm^{-1} and a combination band at 4168 cm^{-1} (Omata et al., 2004).

Quantum Molecular studies serve to confirm the validity of the defect simulations but provide additional information on the electronic structure that is inaccessible to atomistic simulations. Quantum Molecular dynamics simulations have been carried out to calculate the diffusion coefficients and activation energies of protonic defects in $BaZrO_3$. The study on the physical processes and interatomic interactions which significantly contribute to the activation energies in cubic perovskite $BaZrO_3$ showed that the hydrogen bond interactions results in a shortening of the $O\text{-}H^{\cdot}_0 - O_0^x$ separation distance of the eight neighbouring oxygen atoms. The oxygen separation length of the hydrogen bonded complex was found to be 270 pm, which is a significant reduction from the experimental value of 296 pm. The type of proton transfer is purely intra-octahedral. (Munch et al., 2000)

2.3 Proton conducting perovskites

The ideal perovskite-type oxide has the general formula ABO_3, where A represents a large cation, e.g. $Ba^{2+,}$ Sr^{2+} or $Ti^{3+,}$ and B represents a small transition metal/main group ion, e.g. $Cu^{2+,}$ Cr^{3+} or $Sn^{4+.}$ The coordination geometry of the B site ions is octahedral while the A ions are 12-fold coordinated; hence the structure may be described as a framework of corner-sharing BO_6 octahedral containing 12-fold coordinated A site ions. Johnson et al (2005). The structure is schematically illustrated in figure 2.1. The wide range of cation sizes and number of possible valences that can be incorporated into this structure form an enormous number of different perovskites. However, the ideal structure is only observed if the sizes of the cations are within a certain range. This can be checked by the Goldschmidt factor, which is an indicator for the stability and distortion of the perovskite structures. Cubic perovskites like $BaZrO_3$ have a Goldschmidt factor between 0.9 and 1 while orthorhombic like $CaZrO_3$ have a Goldschmidt factor in the range 0.71 to 0.9. This Goldschmidt factor is determined by the sizes of the A site and B site ions relative to each other. It is obtained using the equation:

$$t = (r_A + r_O)/\sqrt{2}(r_B + r_O) \qquad 2.1$$

where r_A, r_B and r_O are the respective radii of A cation, B cation and O anion in the appropriate coordination. (Shannon, 1976; Wikipedia, 2012)

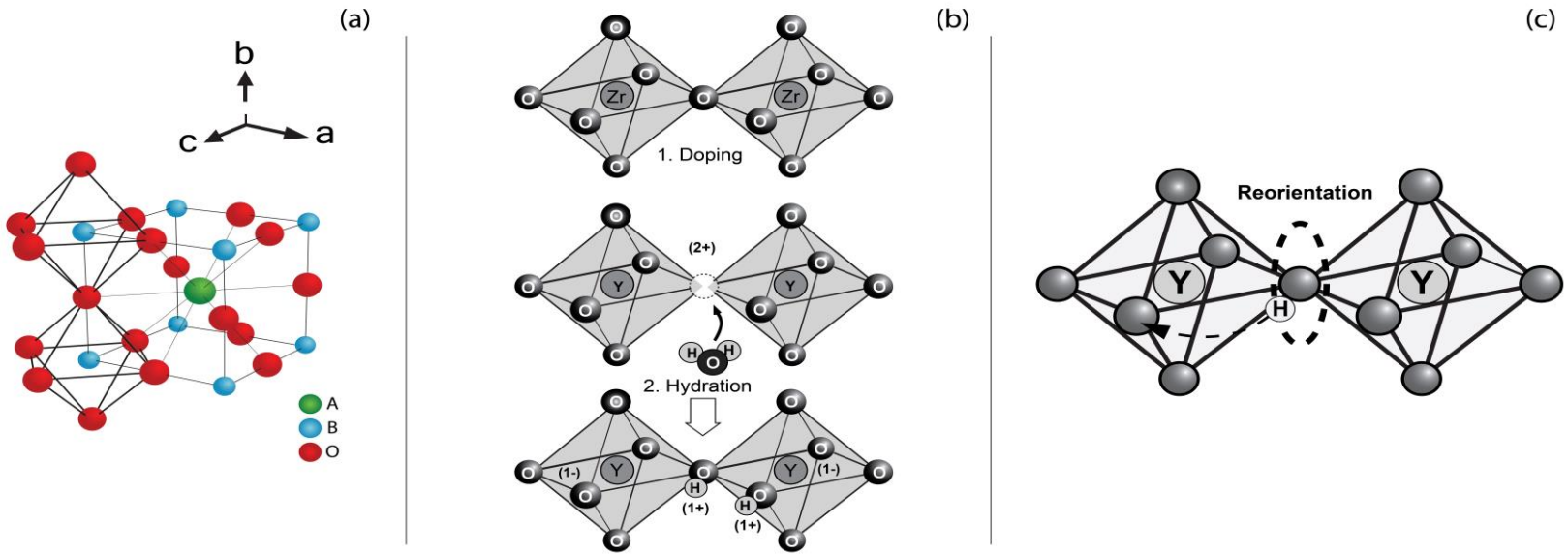

Figure 2.1: a: The ideal cubic ABO_3 perovskite structure showing the octahedral coordinated B ions and the 12-fold coordinated A ions, b: A schematic of the formation and filling of an oxygen vacancy by substituting the octahedral Zr^{4+}-site with a lower-valent Y^{3+} ion followed by hydration and c: A schematic picture of the Grotthuss mechanism in hydrated perovskites. The proton transport is divided into proton transfer between neighbouring oxygen's and reorientation of the hydroxide ion at the oxygen site.

2.3.1 Incorporation of protons in the perovskite structure

High proton conduction in perovskites requires both a high concentration and a high mobility of protons. However, protons are not there inherently, but they can be incorporated into the perovskite structure by forming oxygen vacancies, followed by hydration (Karlsson, 2005). The general formula of such oxygen deficient structures may be written as $A(M_xB_{1-x})O_{3-x/2}$, where M is the trivalent cation substituted on the tetravalent B site.

Water molecules at the gas phase then dissociate into hydroxide ions and protons during hydration, the hydroxide ions fill the oxide ion vacancies where protons form a covalent bond with lattice oxygen. In the Kröger-Vink notation (Kreuer, 2003) this reaction is,

$$H_2O+V_o^{\bullet\bullet}+O_o^{x} \Leftrightarrow 2O\text{-}H_o^{\bullet} \qquad 2.2$$

where two positively charged protonic defects (O-H**.**) are formed. The higher the concentrations of oxygen vacancies in the dry state the higher the proton content after protonation. Thus, the dopant level can control the concentration of protons, as the dopant level determines the concentration of oxygen vacancies in the dry sample. A schematic illustration of the principle with formation of oxygen vacancies and hydration is depicted in Figure 2.1(b).

2.3.2 Proton transport mechanism

The proton conduction mechanism in perovskites is Grotthuss-like, separated into (i) proton transfer between neighbouring oxygen and (ii) reorientation of the hydroxide ion at the oxygen site (Figure 2.1 c). The proton transfer is affected by the degree of hydrogen bonding between the proton and the adjacent oxygen it will jump to. The probability for proton transfer is affected by proton vibration motion and the oxygen lattice dynamics close to the proton (Kreuer, 1999), and in particular by the O-B-O bend mode, which may be seen as a precursor for the proton transfer (Munch, 1996).

Fluctuations in the oxygen separation distance and in the O-H distances may therefore result in the formation of stronger hydrogen bonds during short time periods, which would favour proton transfer (Kreuer, 1999 and 2000). The reorientation step is also affected by the dynamics of the oxygen atoms since it is facilitated by increasing O-O separations, thus lowering the hydrogen bond interaction to neighbouring oxygen event (Munch, 1996). However, a frequency-shift towards a lower frequency of the O-H stretch band in the IR-spectra for several perovskites indicates strong hydrogen bonding, which should favour fast proton transfer rather than fast reorientation of the hydroxyl groups, which requires the breaking of such bonds. The rate-limiting step may be different in different kinds of perovskites and is a topic not yet fully understood (Kreuer, 2003).

The majority of perovskites are oxygen ion conductors at high temperatures above 800 $^{\circ}$C and proton conduction in a certain temperature range is often a competing process with the oxygen conduction. As a consequence, even though the proton conduction starts to decrease as a result of dehydration at high temperatures, the total conductivity may still be high (Karlsson 2005).

2.4 Theory of Experimental Techniques

2.4.1 Powder X-ray Diffraction

X-ray powder diffraction (XRD) is an analytical technique used for phase identification and determination of unit cell dimensions of crystalline materials. XRD yields the atomic structure of materials and is based on the elastic scattering of x-rays from the electron clouds of the individual atoms in the material under investigation. These scattered x-rays produce a Bragg peak if their reflection from the various planes interferes constructively. The interference is constructive when the phase shift is a multiple of 2π and Bragg's law expresses this condition as:

$$n\lambda = 2dsin\theta \qquad 2.3$$

where n is an integer number of wavelengths in path length, λ is the wavelength of the incident radiation, d is the perpendicular spacing of the crystal lattice plane

and θ is the angle of incidence as seen in figure 2.2.

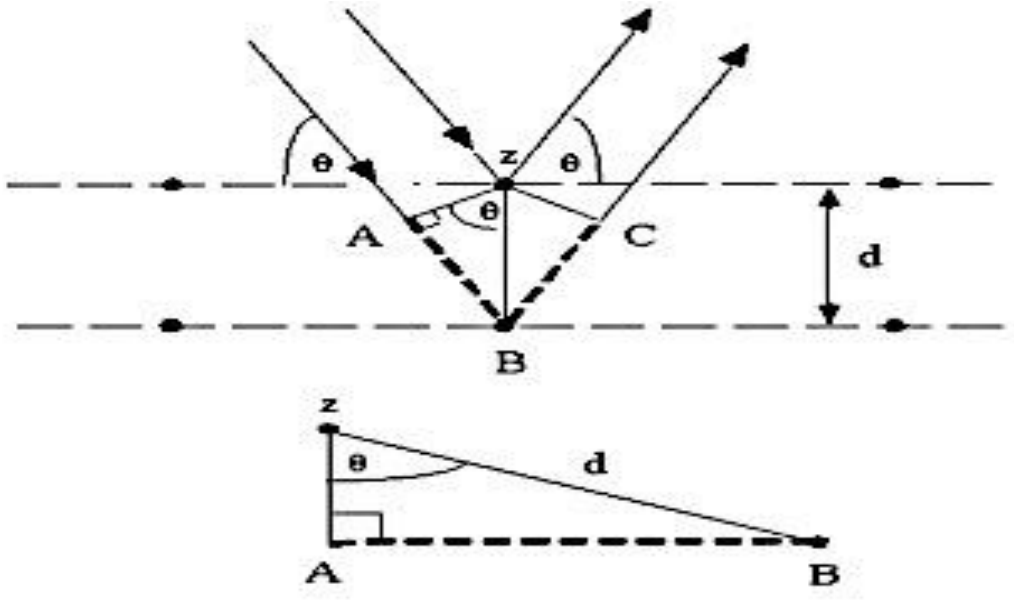

Figure 2.2: Schematic representation of Bragg reflection. AB+BC= multiples of nλ. Constructive interference occurs only when nλ=AB+BC. Source: PDX, 2012

The diffracted x-rays are detected; processed and counted by scanning the sample through an angle of 2θ (Fig. 2.3), which is achieved by moving the sample. The detector is stationary. The sample is rotated as it interacts with the x- rays. All possible diffraction directions of the lattice should be scanned due to the random orientation of crystallites in a sample. Conversion of the diffraction peaks to *d* spacing allows identification of the element, since each material has a set of unique *d* spacing, and the measured *d* is compared with those in standard reference patterns. (Jenkins, 1995; Tsuji, 2004)

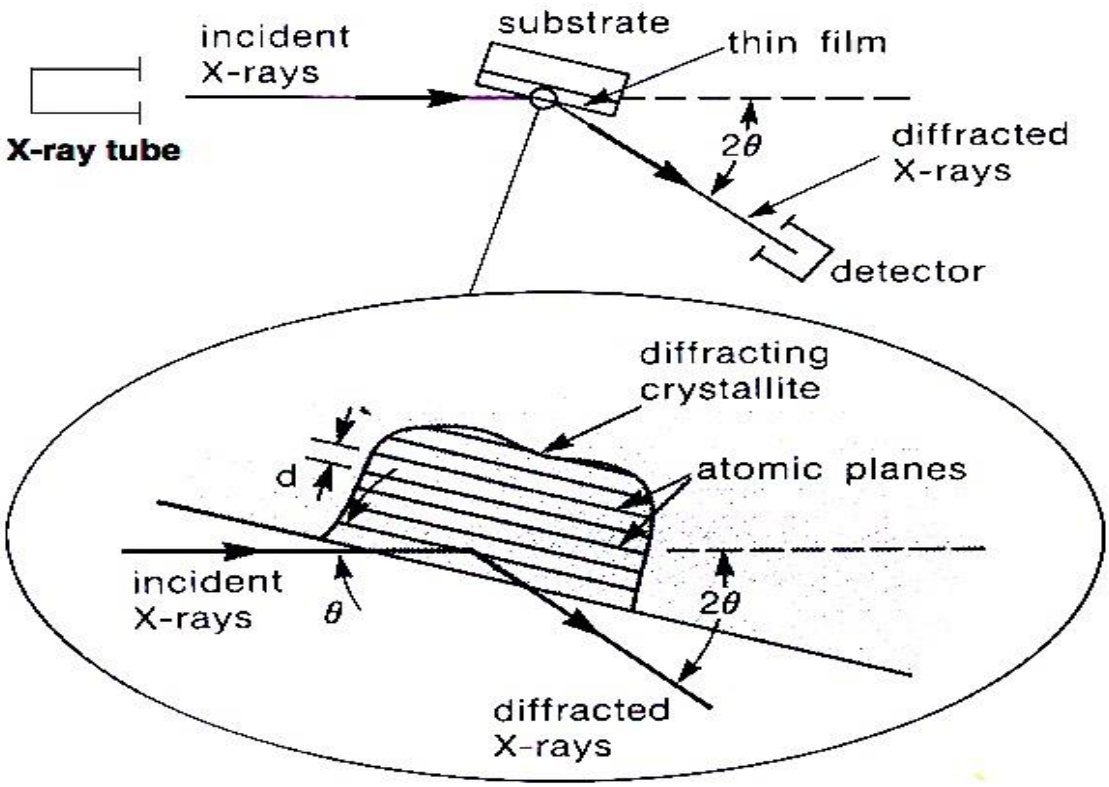

Figure 2.3: Basic features of an XRD experimental set up showing the production, diffraction and detection stages. Source: PDX, 2012

2.4.1.1 Principles of XRD Analysis

The primary characterization of the samples purity, crystal structure and reaction process was performed using the powder x-ray diffraction technique. The sample was irradiated with comparable radiation wavelength to its atomic spacing. Constructive and destructive interference occur between the lattice planes in the crystal, resulting in a diffraction pattern. The pattern presents a detailed picture of the inner structure describable in terms of the symmetry of the unit cell and its dimensions, fractional coordinates and chirality. For an x-ray pattern of a pure material, all its peaks in the diffractogram could be indexed and assigned a space group. Hence this technique is able to fingerprint materials since a materials x-ray pattern is dependent on the atomic number, position of the atoms, and the type of unit cell as well as its size. Despite two or more materials having the same space

group, their diffractograms will be essentially unique. Crystalline materials are characterized by the orderly periodic arrangement of atoms and possess lattice planes (visible from single crystal diffraction data) described by integer values h, k, l known as Miller indices and the parallel distance between two of these planes is denoted d_{hkl}. In reciprocal space the distance is ascribed $1/d_{hkl}$. Given a monochromatic X-ray beam and a set of parallel planes in the crystal, constructive interference will occur if the Bragg conditions are fulfilled. These conditions are: the path length between two constructively interfering waves being a multiple integer (n) of the wavelength and the wavelength (λ) comparable to inter-atomic distances (inter-lattice distances). (PDX, 2012)

2.4.2 Infrared spectroscopy

Infrared (absorption) spectra originate from photons in the infrared region that are absorbed by transitions between two vibrational levels of the molecule in the electronic ground state.

Where $i_o(\nu)$ is the incident beam and $i(\nu)$ is the output beam

The basis of quantitative analyses in Transmission (absorption) spectroscopy is the Lambert-Beer law.

$$A = -\log_{10} T \qquad where \quad T = \frac{I}{I_0} \tag{2.4}$$

Where A is the absorbance, T is the transmittance, I is the intensity of the transmitted beam and I_0 that of the incident beam. (Wikipedia, 2011)

The infrared spectrum is divided into three regions: the near infrared (14000-4000 cm^{-1}), the mid infrared (4000-400 cm^{-1}) and the far infrared (400-10 cm^{-1}). The near

infrared can excite overtones or harmonic vibrations; the mid infrared is used to study fundamental vibrations and associated rotational-vibrational structure. The far infrared has low energy and is applied in low frequency rotational studies as well as in low frequency lattice vibrations. (Wartewig, 2003)

ABO_3 perovskites of cubic symmetry have three sets of triply degenerate infrared modes of symmetry $3f_{1u}$ and the silent optically inactive mode of symmetry f_{2u} (Perry et al, 1965). The f_{2u} mode can become optically active on account of distortions of the crystal lattice of cubic structures. Any perturbation in the structure puts the degeneracies in all modes. When the inactive torsional f_{2u} mode becomes active, the B cation can no longer be the centre of symmetry. This is realized when the lattice is slightly sheared since Active vibrational modes are observed when the lattice is sheared.

2.4.2.1 Principles of Infrared Spectroscopy

Fourier transform technique is the most commonly used infrared technique. The basic component behind Fourier transform infrared (FTIR) spectroscopy is the Michelson interferometer (Fig 2.4), which modulates the infrared radiation emitted from a broadband source to an interferogram. The broadband source is typically made of a ceramic material, and in this work a Globar (SiC) source was used. The Globar operates around 1200–1300 $^{\circ}C$ and emits about 75% of what a black body would emit. The Michelson interferometer consists of two mirrors, a fixed mirror and a moving mirror, and a beam splitter. The mirror moves at a fixed rate. Its position is determined accurately by counting the interference fringes of a collocated Helium-Neon laser. The Michelson interferometer splits a beam of radiation into two paths having different lengths, and then recombines them. A detector measures the intensity variations of the exit beam as a function of path difference. A superposition of wavelengths enters the spectrometer, and the detector indicates the sum of the sine waves added together. The difference in path length for the radiation is known as the retardation δ (δ = OM-OF). When the retardation is zero, the detector sees maximum intensity since all wavenumbers of radiation add constructively. When the

retardation is l/2 of the initial radiation, the detector sees a minimum. An

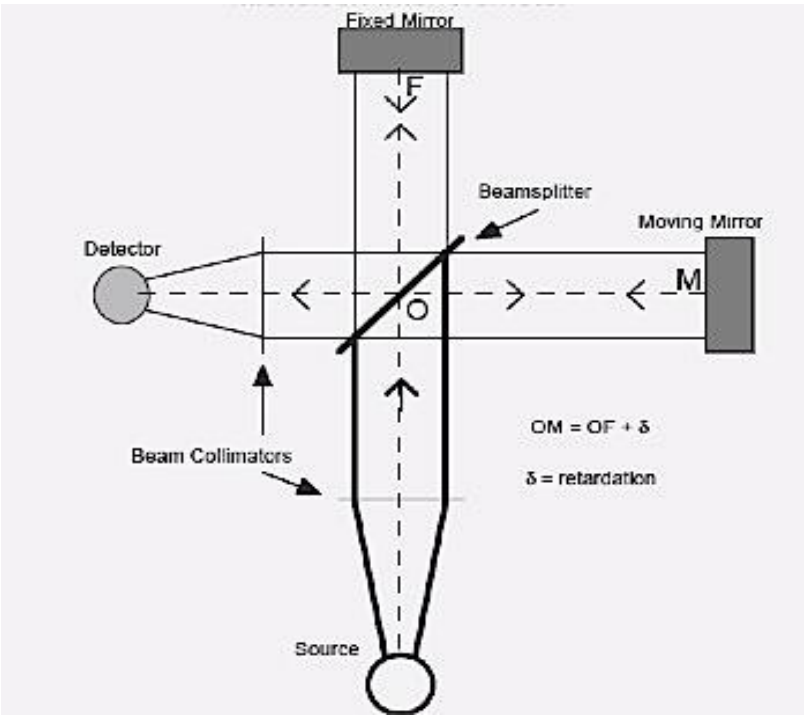

Figure 2.4: The setup of FTIR using a Michelson interferometer.. The sample is between the beam collimator and the detector. Source: UNR, 1998

interferogram is the sum of all of the wavenumber intensities. The interferogram is directed towards the sample, which absorbs characteristic wavelengths depending on its microscopic structure and composition. A detector registers the intensity of the infrared beam, which can be a thermal detector (*e.g.* Deuterated TriGlycerin Sulphate, DTGS) or quantum type (*e.g.* Mercury Cadmium Tellurium, MCT). The thermal detector feels the change in temperature due to the absorption of infrared radiation while in the quantum type detects the infrared radiation excites electrons from the valence band to the conduction band. Quantum detectors need to be cooled for high sensitivity. Finally, computer software transforms the interferogram to the resulting vibrational spectrum. The processing uses the Fourier transform algorithm (Larkin, 2011)

Chapter 3

Experimental techniques

3.1 Introduction

To address the key fundamental question of this study, the effect of increasing dopant concentration on local structure of the perovskite, a combination of methods were used. Samples were prepared by sol-gel method and the initial characterization of the average structure carried out using x-ray diffraction (XRD). Infrared and luminescence spectroscopy were used to characterize the local structure. The sample experimental aspects are examined below.

3.2 Sample preparation

The hydrated perovskites ($BaY_xZr_{1-x}O_{3-x/2}$, $SrY_xZr_{1-x}O_{3-x/2}$ and $CaY_xZr_{1-x}O_{3-x/2}$) investigated in this work were prepared in accordance with the sol-gel technique described by D'Epifanio et al. (2007). It is a wet chemistry process that involves mixing stoichiometric amounts of reactants, and subsequent firing and grinding where citric acid is the chelating agent and ethylene glycol is the solvent.

3.2.1 Synthesis of 20% Y doped $BaZrO_3$

In preparation of 20% Y doped $BaZrO_3$, the mixture compounds were: Ba $(N0_3)_2$ of 99.999% purity and a molar weight of 261.35 g, Zr $(C_5H_7O_2)_4$ of 98% purity and molar weight of 487.216 g and Y $(NO_3)_{3.5}(H_2O)$ of 99.99% purity and a molar weight of 364.902 g from sigma Aldrich.

The reaction equation was:

$$Ba(N0_3)_2 + 0.8\ (Zr(C_5H_7O_2)_4) + 0.2\ (Y(NO_3)_3.5H_2O) \rightarrow BaY_{0.2}Zr_{0.8}O_{2.9} \qquad 3.1$$

The amount of compounds used in the mixture was measured using an electronic balance with a sensitivity of 0.1 mg and the metal compounds were reduced by a factor of 150 from their molar weight to synthesise a manageable sample. The amount used in the synthesis were as follows:

$Ba(N0_3)_2$: 261.35 g/ 150 = 1.7423 g ; $Zr(C_5H_7O_2)_4$: (487.216 g/150) * 0.8 = 2.5985 g; $Y(NO_3)_3.5H_2O$: (364.902 g/150) * 0.2 = 0.4866 g, 60 ml of ethylene glycol and citric acid at a ratio of 2:1, citric acid to metal cations.

The mixture of metal compounds and citric acid in the ethylene glycol was heated on a hot plate while being stirred using a magnetic stirrer up to a temperature of 150 ˚C. This resulted in all the liquid evaporating giving a dark brown solid. The solid material was ground into a powder using an agate mortar and pestle and then placed in a furnace for 16 h at a temperature of 200 ˚C. After cooling and grinding it was heated at a rate of 5 ˚C min^{-1} up to 800 ˚C and left at that temperature for 5 h before being cooled and ground. The process was repeated for temperatures of 900 ˚C, 1100 and finally 1400 ˚C. Due to the combustive nature of barium at high temperatures, the heating and stirring was done in a gas chamber and attended to throughout. Powder x-ray diffraction patterns were obtained after a heating temperature of 1100 ˚C; the patterns were compared with those in the ICDD database. When impurities were observed, the sample was subjected to further heating at 1400 ˚C for 8 hours; an x-ray pattern was obtained that corresponded to a diffraction pattern of a pure perovskite on the ICDD database. $BaZrO_3$ samples of different Y doping were synthesised including 2.5% Y doped calcium zirconate and 2.5% Y doped strontium zirconate. The stoichiometric formulas of the successfully prepared samples were as follows: $BaZrO_3$, $BaZr_{0.9}Y_{0.1}O_{2.95}$, $BaZr_{0.85}Y_{0.15}O_{2.925}$, $BaZr_{0.8}Y_{0.2}O_{2.9}$, $BaZr_{0.7}Y_{0.3}O_{2.85}$, $BaZr_{0.6}Y_{0.4}O_{2.8}$, $BaZr_{0.5}Y_{0.5}O_{2.75}$, $BaZr_{0.975}Y_{0.025}O_{2.9875}$, $SrZr_{0.975}Y_{0.025}O_{2.9875}$ and $CaZr_{0.975}Y_{0.025}O_{2.9875}$.

3.2.2 Hydration, TGA analysis and vacuum drying

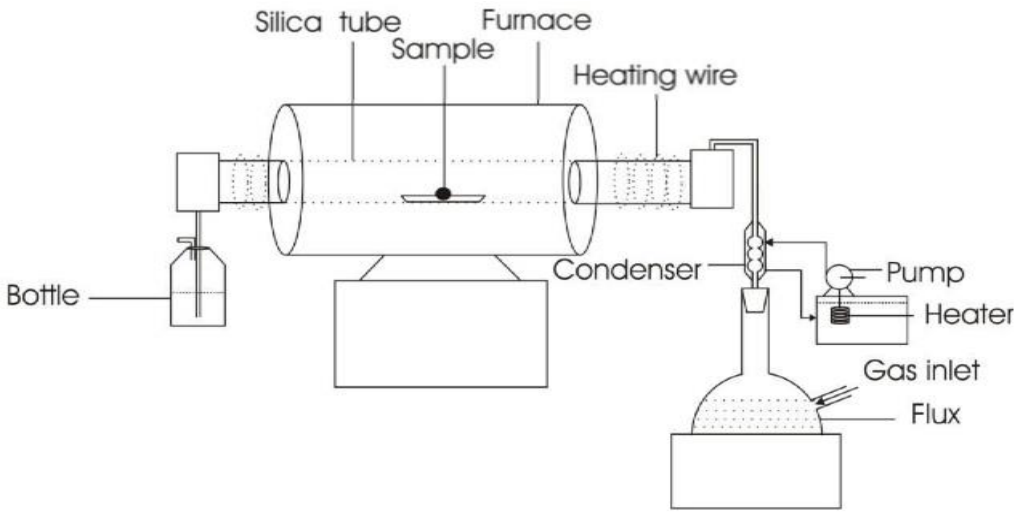

Figure 3.1 Schematic of hydration system setup. Adapted from Ahmed 2008

The synthesized sample was annealed at 500 ˚C in an Ar atmosphere saturated with H_2O vapour at 70 ˚C for 3 days. The hydration setup used is shown in figure 3.1. The level of hydration was assessed using thermo gravimetric analysis (TGA). TGA is an experimental method in which the change in mass of a sample is measured as a function of temperature or time. The change indicates whether the sample has undergone decomposition or absorption on heating or cooling under controlled atmosphere. In the case of decomposition process it is possible to calculate the type of molecules lost by using chemical knowledge of the sample. The change in mass is an inherent property of the material and can be quantitatively linked to physical or chemical processes occurring in the sample. In the case of proton conductors, during the hydration process, protons and oxygen are incorporated into the structure of the material, which results in an increase in the mass of the sample. When the samples are pre-hydrated a loss in mass is observed upon heating under a dry inert atmosphere. By following the mass change in samples quantitatively, it is possible to

know the amount of protonic defects formed during the hydration process.

Synthesized samples were vacuum dried by annealing them in a vacuum tube for 8 hours under 10^{-6} mbar pressure at 900 ˚C. After vacuum drying, the samples were immediately transferred to an inert environment to limit the uptake of protons. The set up used is shown in figure 3.2.

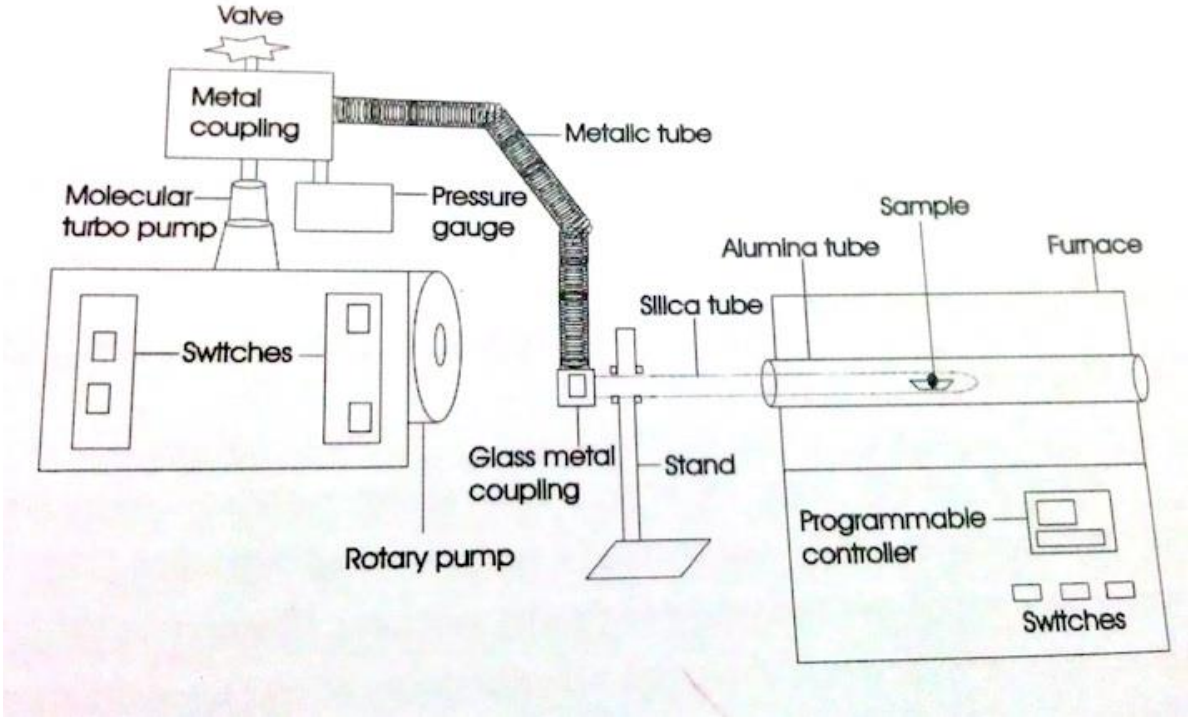

Figure 3.2 Schematic for Vacuum drying setup. Adapted from Ahmed (2008)

3.3 XRD SAMPLE ANALYSIS

The x-ray equipment used in this project was a Bruker D8 AdvanceTM diffractometer with a monochromatic Cu kα x-ray wavelength of 1.5406 Å. The x-ray tube was operated at 40 KV and 40 mA. Intensities were scanned in the 2θ range between 17˚ and 60˚ for set up spectrum collection time 1800 s and the A database (ICDD: International Centre for Diffraction Data) was used to identify the phases

in the sample. The 17˚ to 60˚ range is sufficient to identify a sample as a unique set of peaks of a unit cell of a sample are observed. These scans were carried out after the samples were heated to temperatures of 800 ˚C, 900 ˚C, 1100 ˚C and 1400 ˚C. The obtained XRD patterns were then compared with those in the ICDD database. The samples underwent further calcination until a pure sample was obtained when the perovskite peaks of the synthesized sample corresponded with the expected peaks on the ICDD database.

3.4 Infrared Sample Spectroscopy

Two different Fourier transform IR spectrometers and three different modes of operation were used. The different instruments and modes of operation were required to cover the whole IR spectral range, from 30 to 4500 cm^{-1}, to study the host lattice vibrations in the sample, which gives information of the local structure of the materials.

3.4.1 Low frequency IR measurements

A Bruker IFS 66 V/s spectrometer was used for measurement in the far infrared (FIR) and mid infrared (MIR) region facilitated with a Globar MIR source, and a myler 6-beam splitter at an aperture setting of 10 mm. In the FIR region, 5% of the sample was dispersed in 0.1 g of Polyethylene powder. The mixture was ground in an agate mortar and pestle and then pressed into a 13 mm pellet using a load of 7 tonnes. Polyethylene is transparent to infrared in the region 30-680 cm^{-1}.

In the MIR region, 5% of the sample was dispersed in 0.1 g of potassium bromide (KBr). Mixed using an agate mortar and pestle and then pressed into a pellet using a 13 mm die. KBr is transparent to infrared light in the region 380-7800 cm^{-1}. The KBr beam splitter at an aperture setting of 6 mm was used.

3.4.2 High frequency IR measurement

These measurements were carried out using the diffuse reflectance Fourier transform (DRIFT) mode using a Bruker Alpha instrument to study the O-H stretch region. This mode measures the vibration properties of the sample where the final vibrational spectra are given by the ratio of the logarithm of the reference spectra to sample spectra. In the setup, measurements were done in an inert environment at room temperature on finely ground samples. A reference spectrum was obtained from a gold mirror standard and a KBr beam splitter was used.

3.5 Luminescence spectroscopy

Luminescence spectroscopy gives the symmetry of the local structure of the material. In this study, 1% Europium was placed on the yttrium sites in the 10% Y doped sample. The radius of europium (0.095 nm) is comparable to the radius of yttrium (0.093 nm). From XRD patterns in the ICDD database, the diffraction pattern for samples with 1% Eu on Y sites was similar to those without europium. Therefore introducing europium to the sample was assumed not to distort the local structure of the sample and it was thus used as a tool to investigate the local structure. Eu has an electronic transition of 12000 cm^{-1} for the 0-0 transition, $^5D_0 \rightarrow {}^7F_0$, located between 570 and 580 nm. This transition can be correlated to the number of Eu (dopant atom sites) in the structure. In addition to the synthesising compounds for Y doped barium zirconate samples, Europium (iii) Nitrate ($Eu(NO_3)_3$) of molar weight 337.98 g (sigma Aldrich 99.99%) was added. The samples synthesised were as follows: $BaZr_{0.9}Y_{0.999}Eu_{0.001}O_{3-\partial}$, $BaZr_{0.825}Y_{0.17325}Eu_{0.00175}O_{3-\partial}$, $BaZr_{0.8}Y_{0.198}Eu_{0.002}O_{3-\partial}$, $BaZr_{0.775}Y_{0.22275}Eu_{0.00225}O_{3-\partial}$, $BaZr_{0.75}Y_{0.2475}Eu_{0.0025}O_{3-\partial}$, $BaZr_{0.7}Y_{0.297}Eu_{0.003}O_{3-\partial}$, $BaZr_{0.6}Y_{0.396}Eu_{0.004}O_{3-\partial}$ and $BaZr_{0.5}Y_{0.495}Eu_{0.005}O_{3-\partial}$. Their purity was determined by using x-ray diffraction. Part of the samples was hydrated and part vacuum dried so that tests were carried out on both sets of samples for comparison. Sample luminescence spectroscopy was carried out at University of Verona in Italy where 0.1 g of each dried and hydrated sample was appropriately packaged and sent.

Chapter 4

Results and Discussion

4.1 Introduction

This chapter presents analytical results from the synthesized $BaZr_{1-x}Y_xO_{3-x/2}$ (x= 0.1, 0.15, 0.2, 0.3, 0.4, 0.5) and $AZr_{1-x}Y_xO_{3-x/2}$ (x= 2.5, A=Ba, Sr or Ca) materials. The results include synthesis from XRD, IR spectroscopy and luminescence spectroscopy.

4.2 Material synthesis

The following perovskite samples were synthesised: x= 0.1, 0.15, 0.2, 0.3, 0.4, 0.5 for $BaZr_{1-x}Y_xO_{3-x/2}$ and x= 2.5, A=Ba, Sr or Ca for $AZr_{1-x}Y_xO_{3-x/2}$. During the synthesising process (Figure 4.1), there were observable colour changes as the chemical reaction took place leading to the formation of the perovskite. After a heating temperature of 500 ˚C, a brown solid containing organic compounds was obtained however the perovskite structure was yet to be formed. After a heating temperature of 800 ˚C, the solid colour changed to black and this was attributed to presence of carbon in the solid. A single-phase white perovskite was obtained after a final heating temperature of 1400 ˚C and the structure of perovskite was ascertained using XRD analytical method. Weight loss was noted after subsequent heating temperatures.

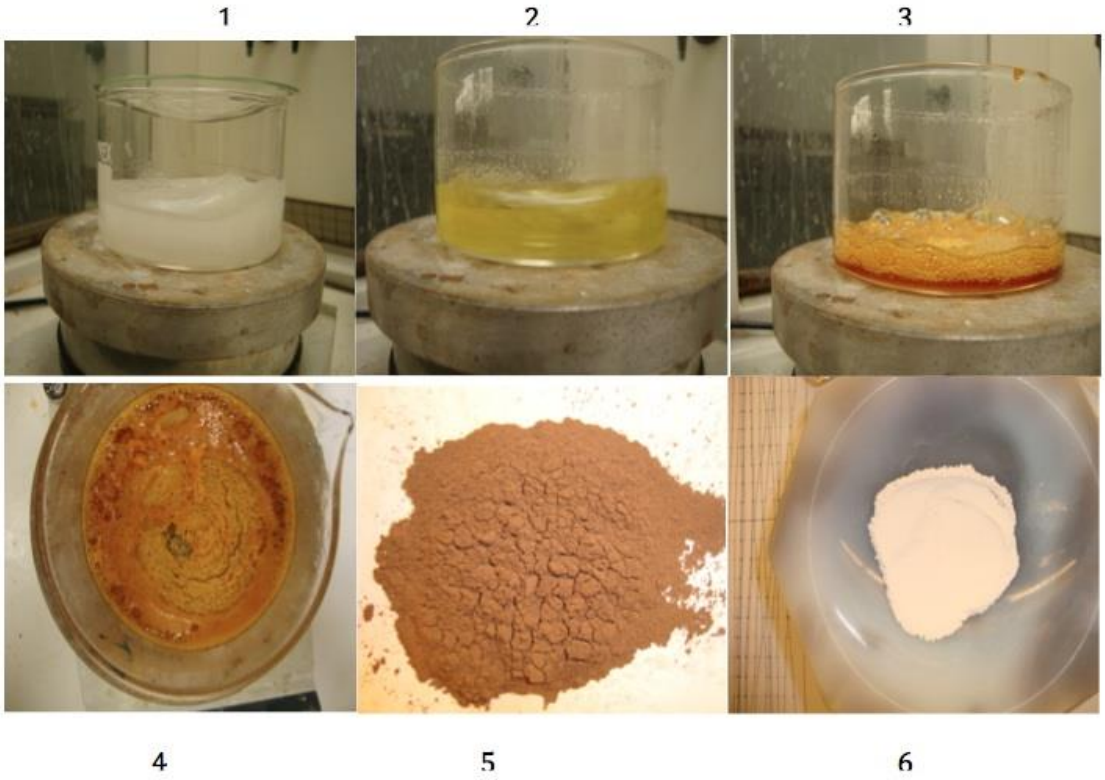

Figure 4.1: Image showing the synthesis process. (1) Mixing of the compounds using ethylene glycol as a solvent, heating at 150 ˚C and stirring using a magnetic stirrer. (2) and (3) shows changes in colour as the chemical reaction takes place. (4) A brown solid obtained after all the liquid has evaporated. (5) Brown powder after heating at 800 ˚C for 5 h and (6) Powder obtained after a final heating temperature of 1400 ˚C for 5 h.

The results obtained from TGA analysis are shown in figure 4.2 where the sample denoted x = 0 had a 0% mass loss. The percentage mass loss increased with increase in dopant concentration except for the sample with doping of x = 0.2. The loss in sample x = 0.2 was less than that from the x = 0.1 and x = 0.15, thus the loss was less than expected in view of the observed trend. The observation was seen as due to a possible ordering of yttrium in the structure of sample x = 0.2 and due to the dopant or vacancy ordering, there could be possible trapping of water in the structure that may have been retained in the sample. The TGA results showed increase in dopant

concentration lead to an increase in the number of vacancies.

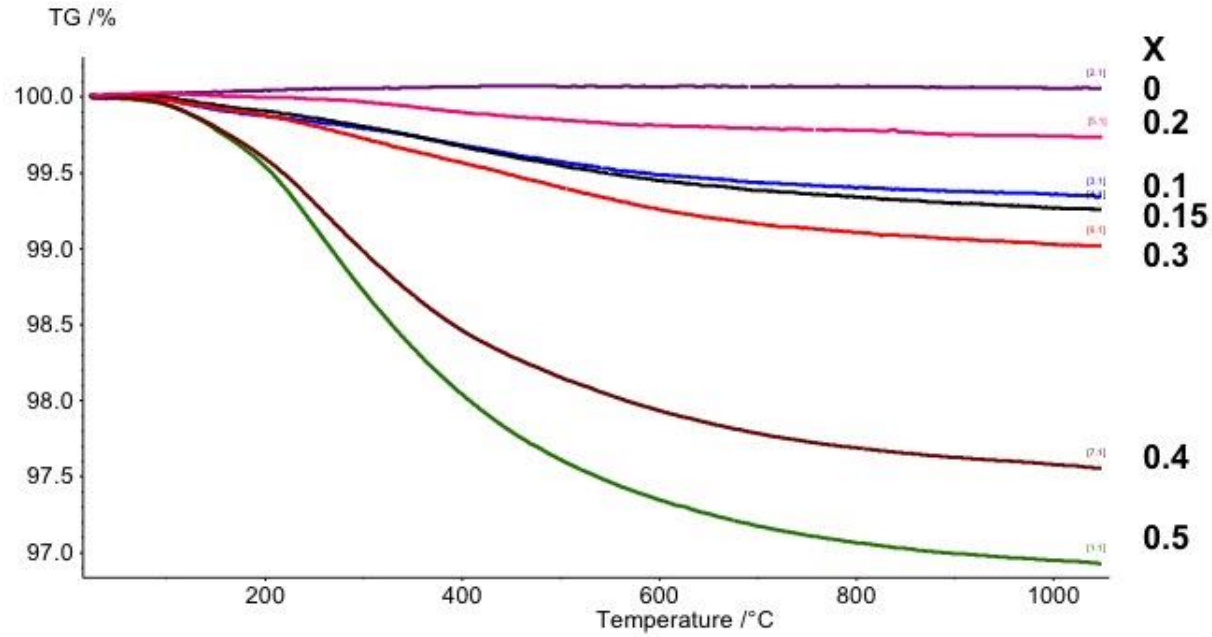

Figure 4.2: Results of TGA analysis of the hydrated samples of $BaZr_{1-x}Y_xO_{3-x/2}$ (x= 0.1, 0.15, 0.2, 0.3, 0.4 and 0.5). The vertical scale is in % and horizontal in ^{0}C.

4.3 Powder x-ray diffraction

To study the average structure of the synthesized samples, a powder x-ray diffraction technique was used. Figure 4.3 shows the x-ray diffraction pattern for $BaZr_{1-x}Y_xO_{3-x/2}$ (x= 0.1, 0.15,0.2, 0.3, 0.4, 0.5 and 0.6). The pattern is that of a cubic structure (ICDD database) with the main perovskite peaks being at 21.4˚ (100), 30˚ (110), 37˚ (111), 43˚ (200), 48.5˚ (210) and 53˚ (211). This is after a final sintering temperature of 1400 ˚C for 5 h.

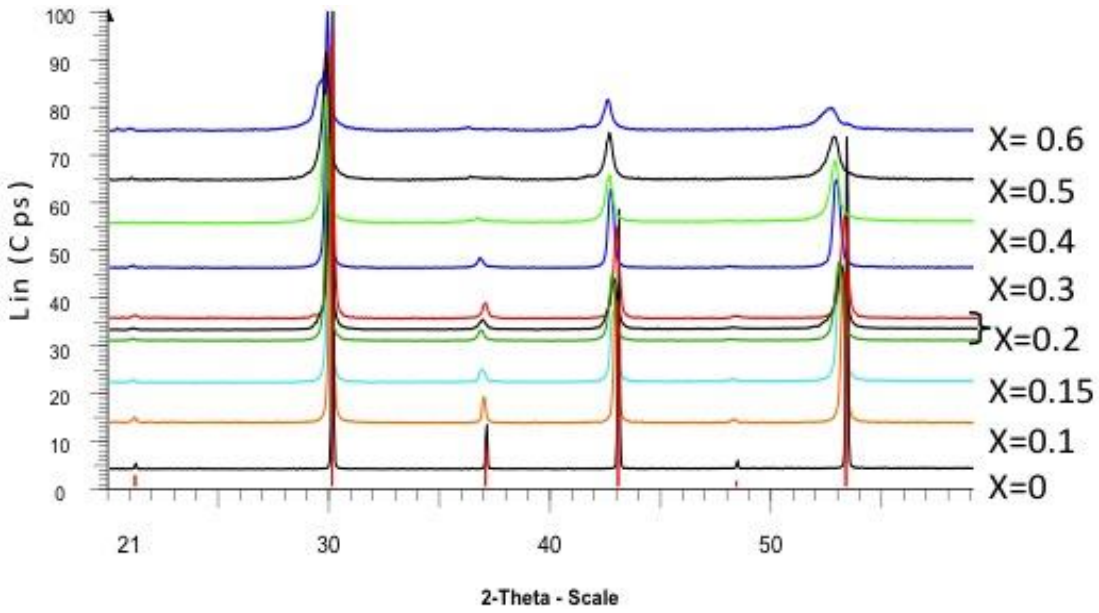

Figure 4.3: XRD pattern for $BaZr_{1-x}Y_xO_{3-x/2}$ (x= 0.1, 0.15, 0.2, 0.3, 0.4, 0.5 and 0.6) after a final heating temperature of 1400˚C for 8 h. The patterns have been vertically offset for clarity and arranged in increasing Y-concentration.

The results were in agreement with those reported by Fabbri et al. (2010), D'Epifanio et. al. (2007) and Bi et al (2011) using the sol gel synthesis method. The ICDD database was used to confirm the average structure of the perovskite. The expected peaks for a cubic barium zirconate structure were observed at the expected diffraction angles. The response intensity decreased at 2θ = 21.4˚, 37˚ and 48.5˚ with increasing dopant concentration. For the x=0.3, x=0.4, x=0.5, x=0.6 patterns, the 48.5˚ peak is not observed. The 30˚, 43˚ and 53˚ perovskite peaks were observed in all the samples, however, as the doping was increased, the perovskite peaks broadened and shifted towards the lower 2θ. This was attributed to an increase in unit cell parameters due to the larger ionic radius of the dopant (Y^{3+}-0.093nm) compared to that of the B site atom (Zr^{4+}- 0.079nm). Calcium zirconate, strontium zirconate and barium zirconate doped with 2.5% yttrium were also synthesized using the sol gel technique. The strontium zirconate and calcium zirconate were found to have an orthorhombic structure while the barium zirconate had a cubic structure (Figure 4.4). From the XRD patterns, it was observed that the 110, 210 and 211 lattice parameters

were shifted towards higher 2θ with the decrease in size of the A site atom.

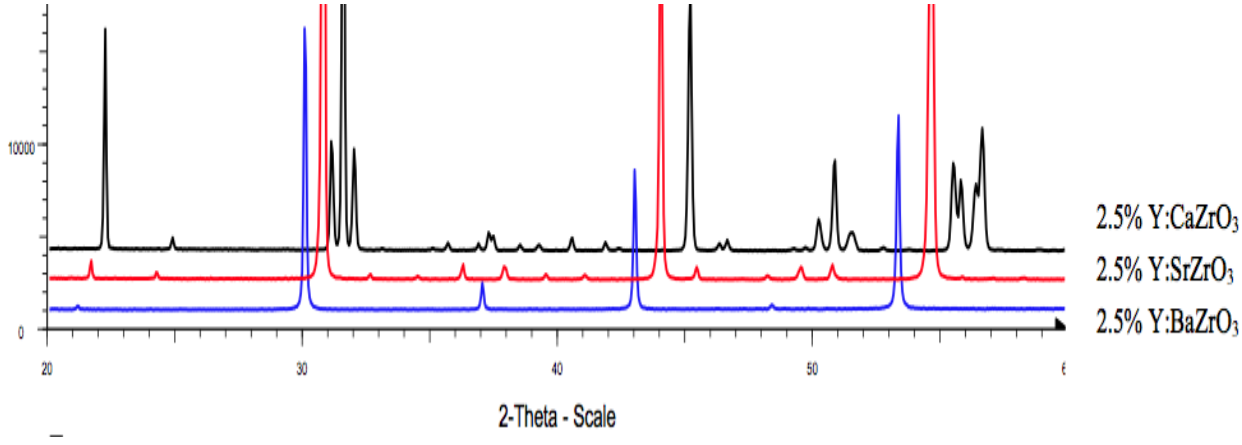

Figure 4.4: XRD patterns for $AZr_{1-x}Y_xO_{3-x/2}$ (x=2.5 and A=Ba, Sr or Ca) after a final heating temperature of 1400 ◦C for 8 h. The patterns have been vertically offset for clarity and cut off at approximately half the peak height.

XRD analysis has the ability to show the long-range average structure of the perovskites while IR and luminescence spectroscopy are able to help identify the short range structure as a function of dopant concentration and hydration.

4.4 Infrared spectroscopy

4.4.1 Low frequency IR region

Figure 4.5 shows the spectra of the dry samples of $BaZr_{1-x}Y_xO_{3-x/2}$ measured in a transmission setup over the frequency region of 50-1000 cm^{-1}. $BaZr_{1-x}Y_xO_{3-x/2}$ samples revealed strong bands at 140 cm^{-1} and 280 cm^{-1} for x= 0, 0.1, 0.15. The x = 0.2 spectrum had strong bands at 140 cm^{-1}, 280 cm^{-1} and weak shoulders at 200 cm^{-1} and 330 cm^{-1}. The x = 0.3, 0.4 and 0.5 had strong bands at 140 cm^{-1} and 330 cm^{-1}. With increasing dopant concentration, the 140 cm^{-1} bands tended to shift towards the lower frequency region as indicated by the lines and the broader peak at

280 cm^{-1} towards higher frequency. Yttrium has a higher ionic radius than zirconium, thus increasing in yttrium concentration leads to a change in the Ba-[ZrO6] cation stretch leading to the position of the peak shifting towards a lower wavenumber. A strong band was observed at 550 cm^{-1} and weak shoulders at 580 cm^{-1} for x = 0, 0.1, 0.15 and 0.2.

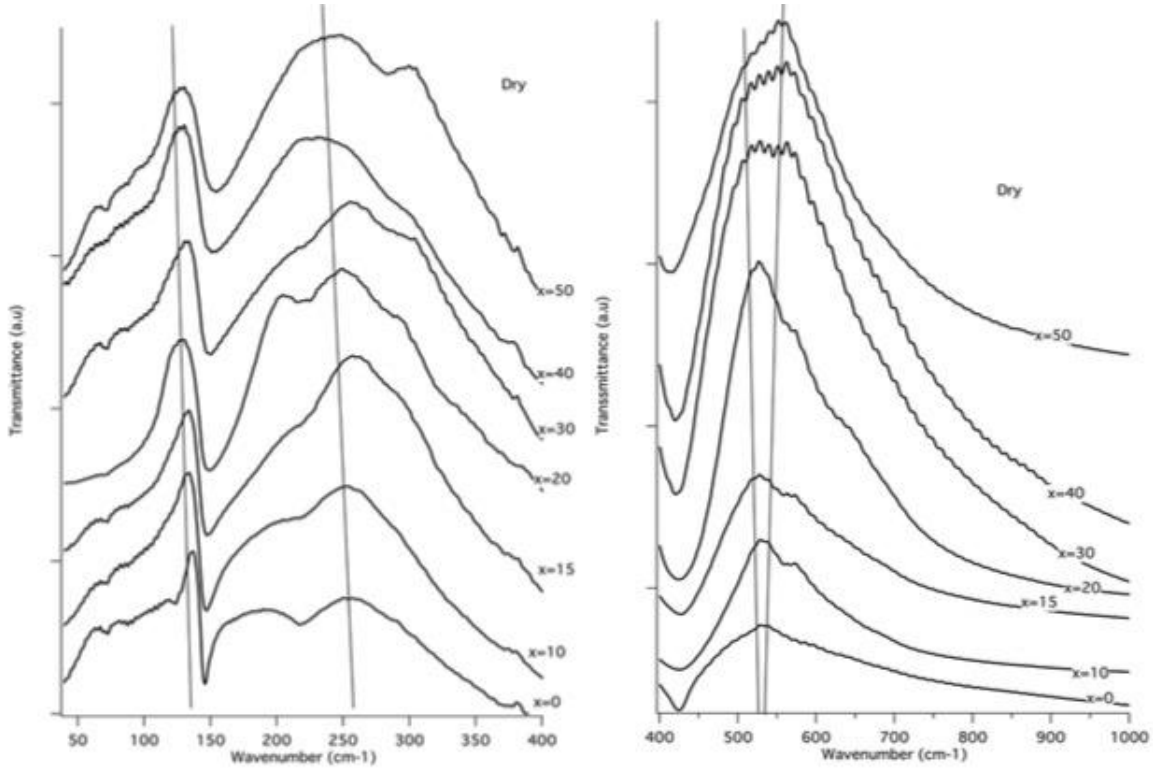

Figure 4.5: FIR and MIR spectra for the $BaZr_{1-x}Y_xO_{3-x/2}$ samples with absorption bands observed at 140 cm^{-1}, 280 cm^{-1}, 330 cm^{-1} and 550 cm^{-1}. The spectra have been vertically offset for clarity

The 140 cm^{-1} band lay in the expected region for the Ba- [ZrO_6] cation stretch, 280 cm^{-1} and 330 cm^{-1} in the O-Zr-O bending range while the 550 cm^{-1} was in the Zr-O stretch vibrations (Last, 1957; Nakagawa, 1967). In the MIR region, the shape of the 550 cm^{-1} band changed in shape with increasing Y-doped concentration. Figure. 4.5 shows the undoped sample had a single peak at 550 cm^{-1} while the 50% Y-doped sample had a broadened peak in the same band. The presence of yttrium can be

attributed to the change from a peak to a band in the O-Zr-O bending range at 550 cm^{-1} Increasing the dopant concentration led to an increase in the average distortion of the structure (Figure 4.5). The 280 cm^{-1} peak for the x = 0.2 sample had strong shoulders at 200 cm^{-1} and 300 cm^{-1}. This could be due to a possible ordering of the Y dopants in the O-Zr-O/ O-Y-O for the x=0.2 sample. The x = 0.3 and x = 0.5 samples had strong shoulders at 300 cm^{-1} wave numbers. The structural distortion was therefore attributed to the different ordering of the B site atoms in the structure. There were three possible ordering in the structure that ultimately affected the structure of the perovskite and they are Zr-O-Zr, Zr-O-Y and Y-O-Y. The Zr-O-Zr and Y-O-Y are symmetrical while the Zr-O-Y is asymmetrical thus leading to a tilt in the octahedral. (Karlsson, 2007; Nakagawa, 1967) The different ordering arrangements present different vacancies and charge concentrations.

In order to investigate the effect of the size of the A site atom, further IR investigations were done for different A (Ba, Sr or Ca) atoms which gave rise to different vibrational spectra. In the near infrared region, a comparison of the spectra of 2.5 % yttrium doped $AZrO_3$ with different A atoms is presented in figure 4.6

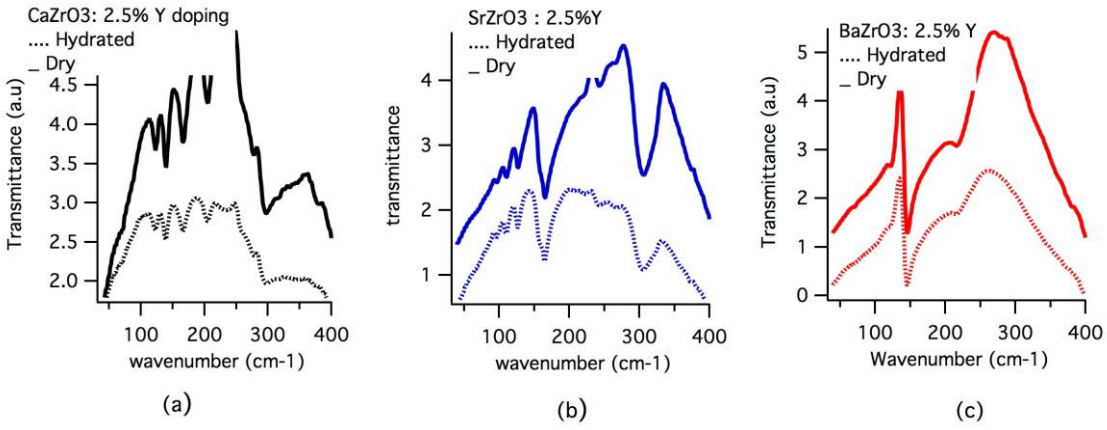

Figure 4.6: Far infrared spectra for dry (continuous) and hydrated (dotted) $AZrO_3$ (A=Ba, Sr or Ca) with 2.5% Y doped samples. a) in the calcium zirconate spectra with 10 main peaks b) is the strontium zirconate spectra with 6 main peaks and c) is the barium zirconate spectra with 2 main peaks.

It was observed that the 2.5% Y doped calcium zirconate, strontium zirconate and barium zirconate had 10, 6 and 2 peaks respectively (Figure 4.6). The A- [ZrO6] cation stretches are found in this region of radiation spectrum and the observed differences in absorption peaks were attributed to the sizes of the A site atoms. The size of Ca^{2+} is 0.099 nm, Sr^{2+} is 0.113 nm and Ba^{2+} is 0.135 nm. The differences were also attributed to the average structure of the perovskite (Figure 4.5) where calcium zirconate and strontium zirconate crystals are orthorhombic while the barium zirconate is cubic.

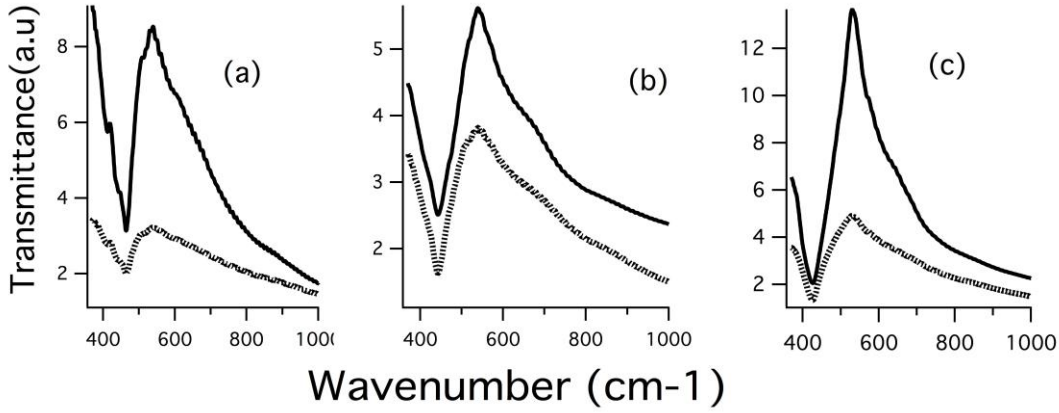

Figure 4.7: Mid infrared region for dry (continuous) and hydrated (dotted) $AZrO_3$ (A=Ba, Sr or Ca) of 2.5% Y doped samples. (a) calcium zirconate (b) strontium zirconate and (c) barium zirconate. A main peak is observed at the 550 cm^{-1}.

In figure 4.7 are the spectra of the mid IR region where we have the Zr-O stretch vibrations. The three samples had a main peak at 550cm^{-1}. Since there were no clear differences between the spectra, it was assumed that the A site atom had no effect on the Zr-O stretch vibrations. However, with no base point to defend these results, further studies and investigation of the effect of the A site atom on the Zr-O stretch vibrations would need to be carried out. In the lower frequency region, it was observed the peaks from the dry samples were sharper than those from the hydrated (4.6 and 4.7). It was therefore easier to resolve the different peaks in figures 4.6 a) and b) for the dry samples than the hydrated samples. This led to a conclusion that

the presence of protons have an effect on the vibrations of the A site ion.

4.4.2 O-H stretch region

The vibrational dynamics of protons in hydrated perovskites are precursors to proton transfer between neighbouring oxygens, which is one of the mechanisms in the long-range diffusion of protons. Understanding of these will hence help in the synthesis of new perovskites with higher proton conductivity and for this purpose IR spectra were measured and analysed for $BaZr_{1-x}Y_xO_{3-x/2}$ and $AZr_{1-x}Y_xO_{3-x/2}$ (x= 2.5, A=Ba, Sr or Ca). The results obtained were compared with observations by Karlsson et al. (2007) for Indium doped $BaZrO_3$.

The O-H stretch vibrations characterize protons in perovskites. They are manifested as a broad band typically in the range 2500-3600 cm^{-1}. This may be compared to the O-H stretch mode of free water molecule at 3657 cm^{-1} (Kreuer, 1999; Omata, 2004; Karlsson et al., 2007). The O-H stretch vibrations in the perovskite structure have a lower frequency than that of a free water molecules that can be attributed to the hydrogen bonding with neighbouring oxygen atoms. (Glerup et al., 2002) The broad nature of the band results from a large variation in the hydrogen bond strength in the perovskite structure as compared to that of a free water molecule.

Figure 4.8 shows evidence that hydration increases the intensity of the O-H stretch band around 3250 cm^{-1}. The O-H stretch band for x = 0 was weak and it was attributed to the absence of protons in the undoped perovskite structure. There was an O-H stretch band at 3250 cm^{-1} on the dry spectra, (figure 4.9) indicating it was not possible to remove the protons completely from the doped samples (Karlsson et al., 2005). Of note though was the absence of the vibrational band at 4250 cm^{-1} in the dry sample. There was a clear change in shape in the O-H stretch absorption region with increasing dopant concentration.

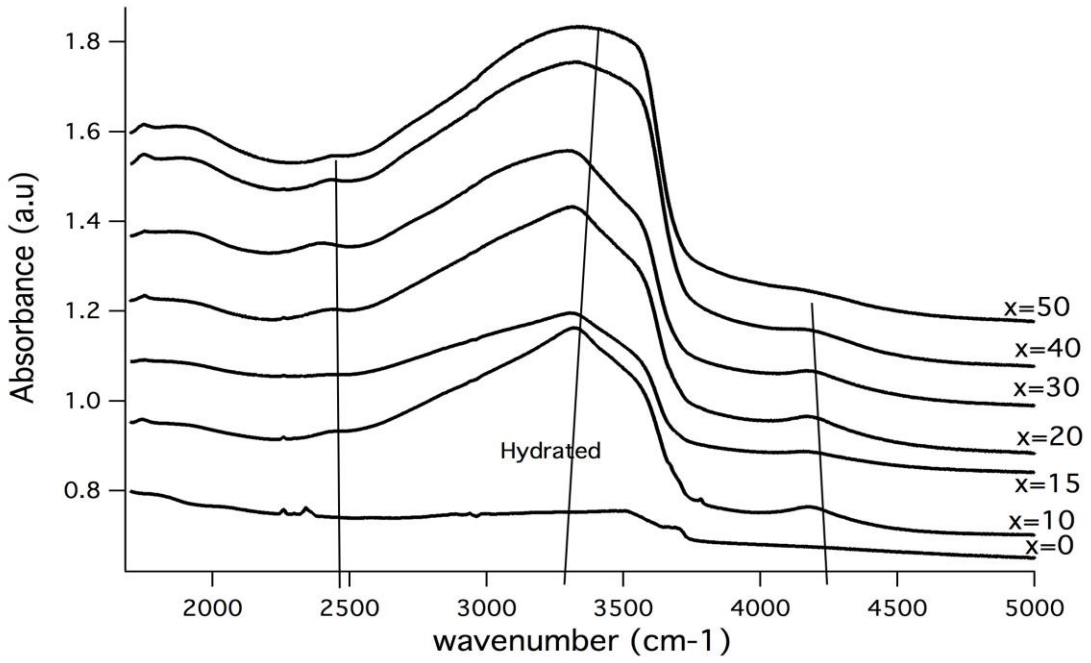

Figure 4.8: Spectra of $BaZr_{1-x}Y_xO_{3-x/2}$ samples in the O-H absorption region. The spectra have been vertically offset for clarity.

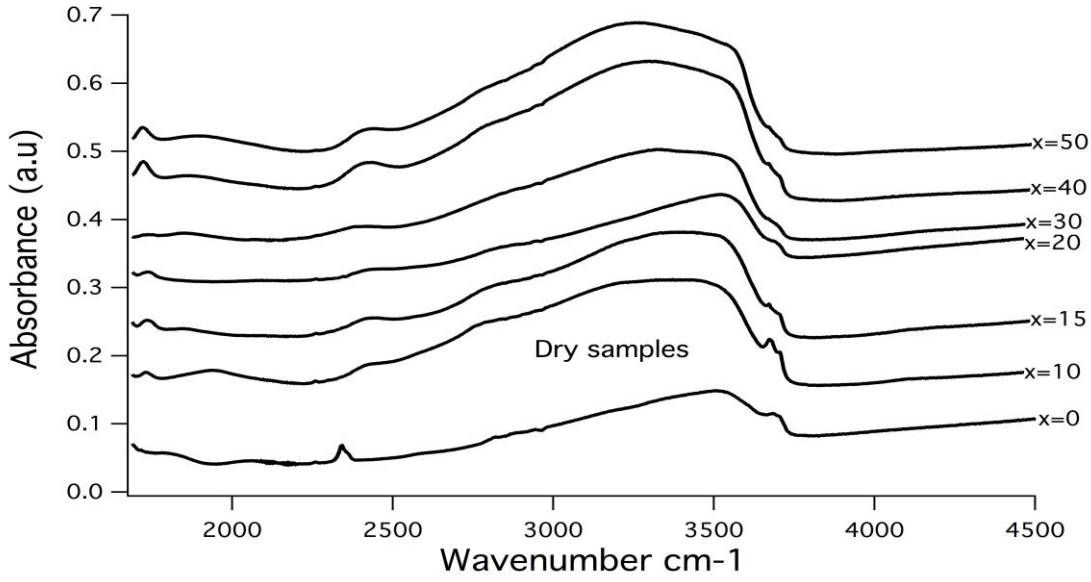

Figure 4.9: Spectra of dry $BaZr_{1-x}Y_xO_{3-x/2}$ samples in the O-H absorption region. The spectra have been vertically offset for clarity.

In the O-H absorption region, the hydrated $BaZr_{1-x}Y_xO_{3-x/2}$ samples had a strong band around 2250 cm^{-1} and 3250 cm^{-1}. The dry spectra had a weak band in the same region (Figure 4.9). The bands at 2000 cm^{-1} and 2500 cm^{-1} increase in intensity with increasing dopant concentration. The 2500 cm^{-1} O-H stretch increases in intensity with increasing dopant concentration. The increase in intensity was in agreement with indium doped $BaZrO_3$ spectra observed by Karlsson et al. (2005) The 2250 cm^{-1} and 3850 cm^{-1} bands broaden with increasing dopant concentration. This implied an increase in the number of oxygen vacancies as the number of dopants increased. With a larger number of oxygen vacancies, there should be more protons incorporated in the structure. There was also a combination stretch and bend band observed at 4250 cm^{-1} (Kreuer, 1999; Glerup et al., 2002).

4.4.2.1 Peak fit analysis of the O-H stretch region

A peak fit analysis of the O-H stretch band was carried out in order to extract more details for investigations of the difference between the six hydrated samples. The peak fit of the 10% Y doped sample is shown in fig. 4.10 c as an example. The deconvolution of the O-H stretch region indicated the preferred sites for the protons. The 2250 cm^{-1} and 3850 cm^{-1} region was resolved into four different bands. During the fitting process, the x position on the Gaussian was fixed for different samples so as to compare their intensities. This enabled the comparison of intensities of the individual bands for the different samples (Fig 4.11 b).

4.4.2.1.1 Spectrum analysis from the O-H region

The spectrum had a region of linear background as shown in figure 4.10 (a). A line was drawn using the equation y= -mx+c joining the lowest position on the curve. (Figure 4.10 (b)). Thereafter, the intensities (y) described by the linear equation were subtracted from the spectrum. The resultant spectrum is shown in figure 4.10 (c) as well as the fitting of the four Gaussian bands. The spectrum was fitted with the customized Gaussian equation:

$$f(x) = a_1 \exp(-\frac{x_1 - x}{b_1})^2 + \cdots + a_4 \exp(-\frac{x_4 - x}{b_4})^2 \qquad 4.1$$

where a_i is the amplitude of the band, x_i is the position of the centre of the peak and b_i is the width of the band. The fitted spectra are in the appendix after subtraction of the linear background as seen in figure 4.11

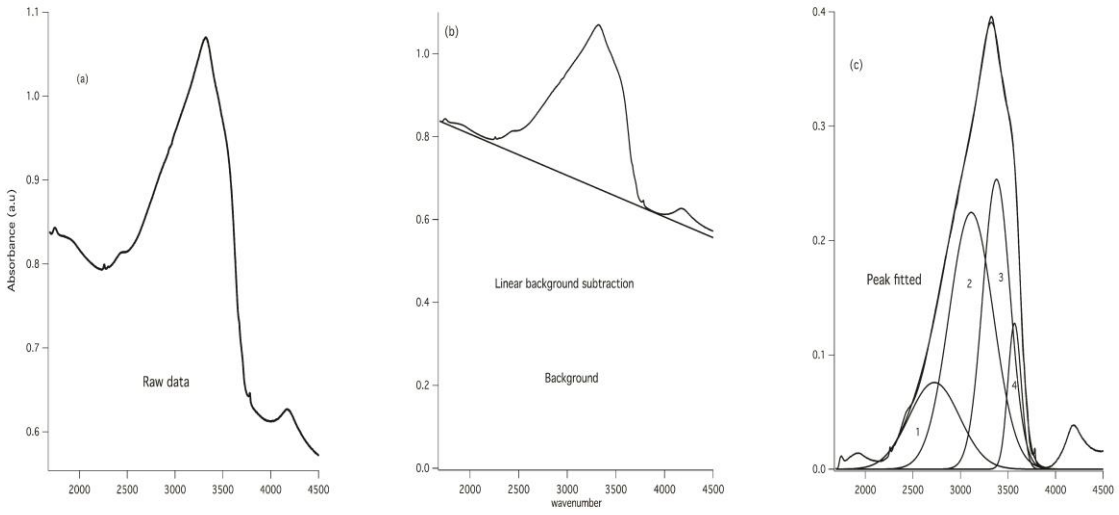

Figure 4.10: Spectrum analysis showing (a) absorbance raw data (b) linearly subtracted background and the background region and (c) peak fitted spectra fitted with four Gaussian bands. The horizontal scale in all spectra is in wave number (cm^{-1})

Subtraction of the background allows ease of spectrum analysis and comparison of intensities for the different dopant concentrations. A stepwise background subtraction and peak fit analysis is shown in figure 4.10. Appendix figure 4 shows the fitted spectrum for the broad O-H peak observed between 2250 cm^{-1} and 3850 cm^{-1}. The region was fitted with four Gaussian bands. It was observed that the band around 4250 cm^{-1} decreased in intensity with increasing dopant concentration. This is likely a combination of the O-H stretch and O-H wags. The four Gaussian bands

fitted well with the experimental spectrum. It may also be attributed to an unrealistic increase in force constant of more than 40 % and a very short distance compared to the 'free' O-H. (Glerup et al., 2002)

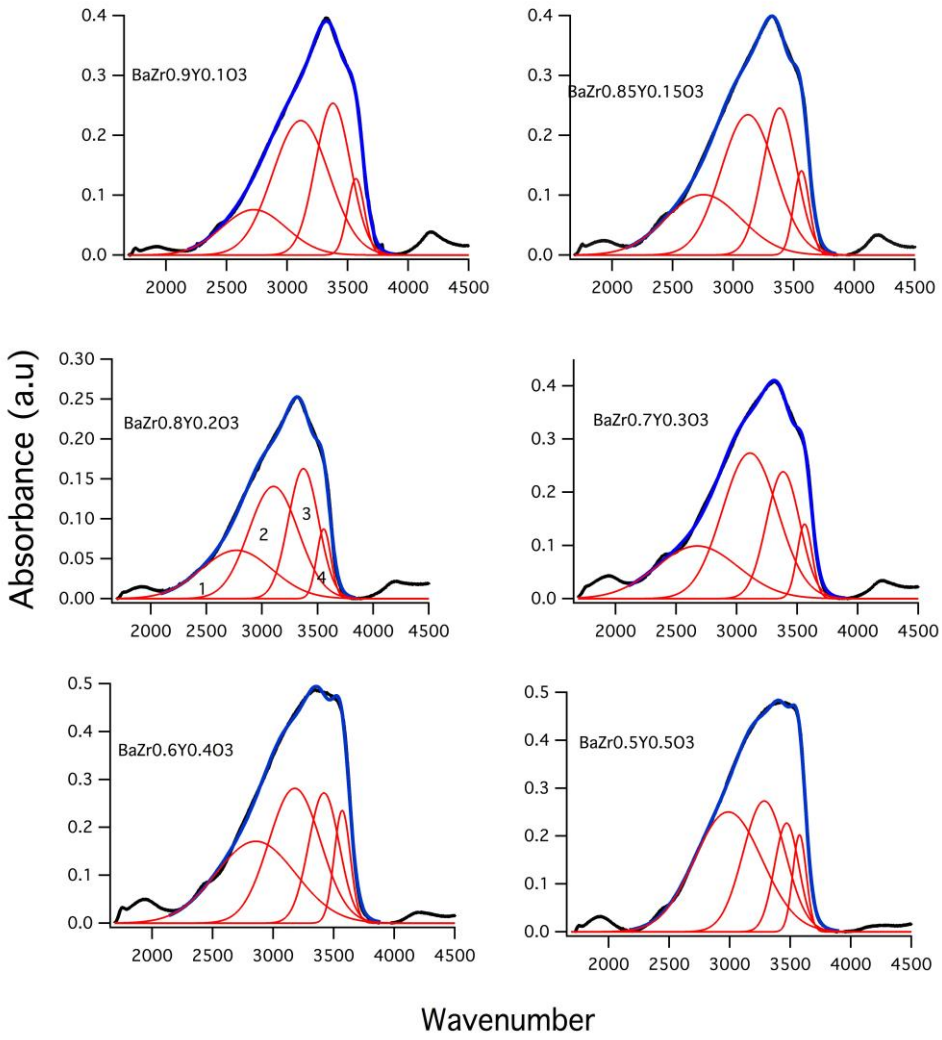

Figure 4.11: Spectra analysis showing the O-H region fitted with four Gaussian bands for $BaZr_{1-x}Y_xO_{3-x/2}$ samples. The horizontal scale in all spectra is in wave number (cm^{-1})

The total area of the O-H region, relative to that of the x = 0.1 sample, increased with increasing dopant concentration except for the x = 0.2 whose area was less

than that for x = 0.1 despite having a higher dopant concentration.

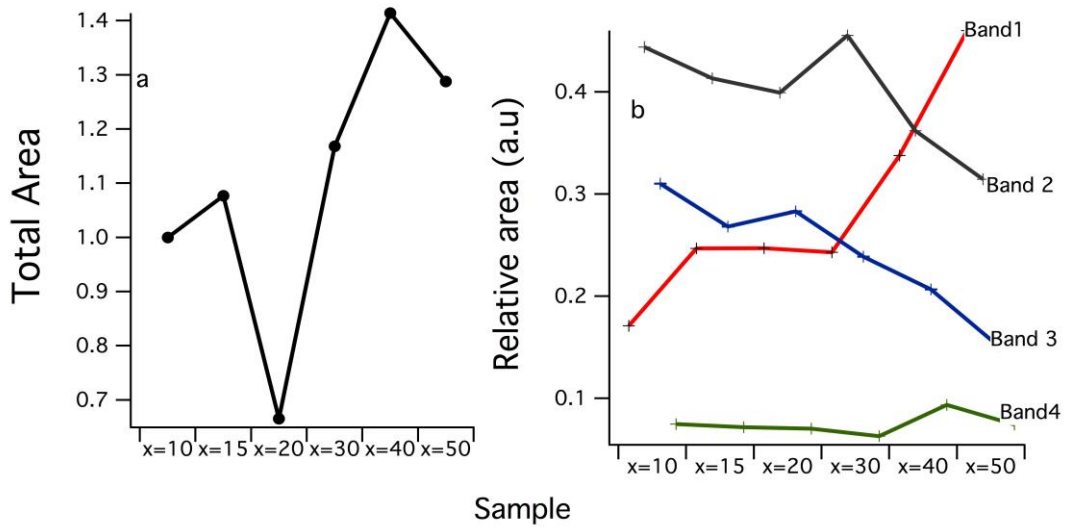

Figure 4.12: Graphs showing a) The total area of the samples relative to that of the x= 0.1 sample and b) The relative area of each of the four Gaussian bands. X is the %age yttrium concentration in the $BaZr_{1-x}Y_xO_{3-x/2}$ samples.

Comparing the relative intensities for individual bands from different samples, it was observed that the total area increased with increasing dopant concentration (figure 4.12 b). For the relative integrated area, band 1 is increased with increasing dopant concentration from absorption wavenumber 2700 cm^{-1}. Band 2 and 3 decreased with increasing dopant concentration from 3100 cm^{-1} and 3400 cm^{-1} respectively, while band 4 did not change significantly with changes in dopant concentration from 3600 cm^{-1}. The frequencies of the four Gaussian fitted peaks (1 to 4) were assessed as follows: bands 3 and 4 they are associated to protons in locally symmetric environments while band 1 and 2 were associated to protons in mixed environments and/or close to an oxygen vacancy. More protons are found in strongly hydrogen-bonded locations and Karlsson et al. (2005) observed this phenomenon in $BaZr_{1-x}In_xO_{3-x/2}$ crystals. Protons have a preference for the lower wavenumber site (2400 cm^{-1}). Ideally the undoped sample has no oxygen vacancies in the structure and therefore no O H stretch band. The IR measurements revealed the details on the

local structure of the perovskite. Luminescence spectroscopy was used to study the behaviour of the dopant in the perovskite. It was also used to show the preferred proton sites in the structure.

4.5 Luminescence spectroscopy

Luminescence spectroscopy was done to compliment the results obtained from the IR spectroscopy. The XRD pattern for $BaZr_{0.9}Y_{0.999}Eu_{0.001}O_{3-\partial.}$ is shown below. The red line show that the obtained pattern was in correspondence with the acceptable standard in the database.

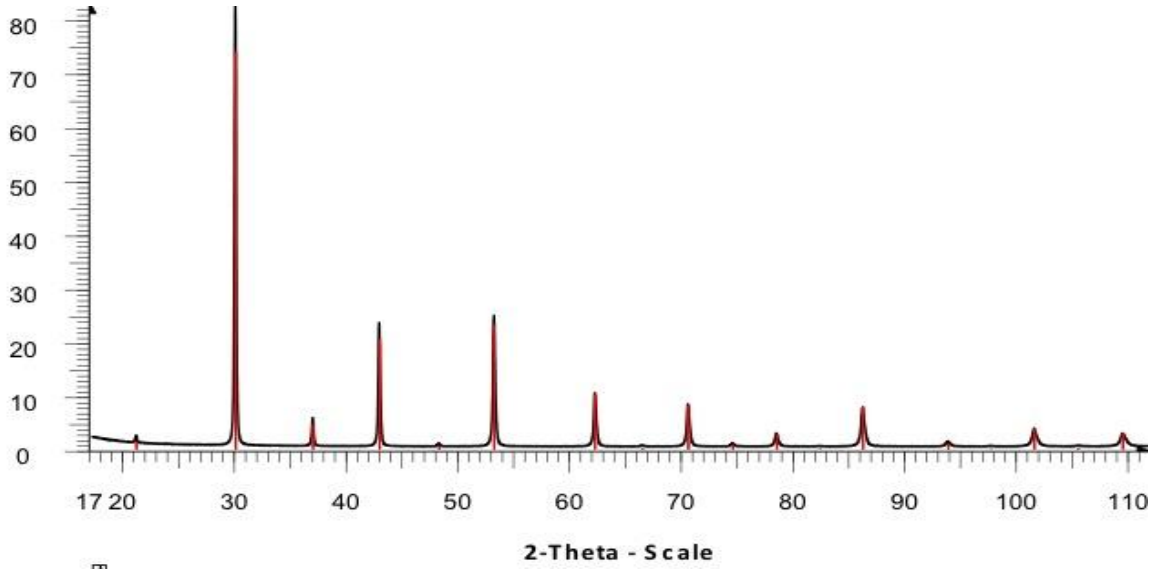

Figure 4.13: X-ray diffraction pattern for $BaZr_{0.9}Y_{0.999}Eu_{0.001}O_{3-\partial.}$ The red lines are from the database for a $BaZr_{0.9}Y_{0.1}O_{3-\partial}$ sample.

Figure 4.14 shows the spectra of both samples (hydrated and dry) measured under excitation by a 473 nm laser excitation at room temperature. There were some differences between them (Figure 4.13), where the normalised intensities are presented. In particular, the 0-0 transitions ($^5D_0 \rightarrow {}^7F_0$, located between 570 and 580 nm) counts the number of sites occupied by Eu^{3+}. It is apparent from Figure 4.13(b) that there were two Eu^{3+} sites in the dry sample and only one in the hydrated

sample. Alarcon et al. (1992) observed two different sites for Eu^{3+} in $BaZrO_3$ co-doped with La^{3+}. This was interpreted as possible occupation by Eu^{3+} on the Ba site and on the Zr site in the structure. The other difference between the two samples is the so-called asymmetry ratio R, defined as the ratio of the integrated intensities of the $^5D_0 \rightarrow {}^7F_2$ and $^5D_0 \rightarrow {}^7F_1$ transitions. The values of R were 7.8 (dry) and 5.5 (hydrated), indicating that on average the geometry of the site(s) accommodating Eu^{3+} is more distorted in the case of the dry sample. The dry sample had two Eu sites, near a vacancy and near lattice oxygen and the hydrated sample there was one Eu site, near lattice oxygen and the proton sits close to the dopant atom.

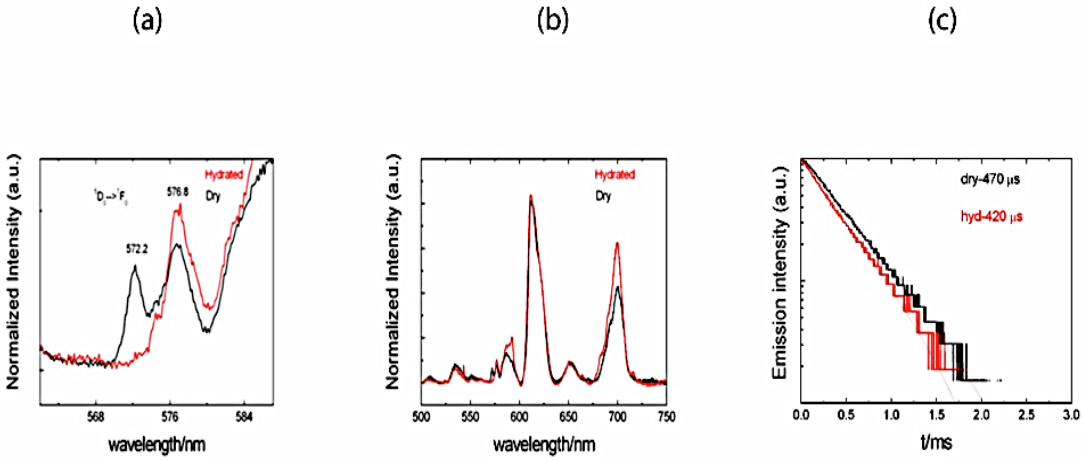

Figure 4.14: Figure (a) showing the electronic transitions (b) Expanded view of the 0-0 transitions upon a 473nm laser excitation at room temperature and (c) Exponential decays for the dry and hydrated sample. The hydrated sample decays faster.

The decay times of the luminescence from $^5D_0$ were measured at room temperature upon pulsed excitation at 532 nm (Figure 4.13(c). The decay curves are almost perfectly exponential. The two samples had a similar decay time, slightly faster in the case of the hydrated sample with the same exponential behaviour. The O H groups are very good quenchers of the luminescence, giving rise to non-radiative relaxation of the emitting level and drastically shortening the decay time. In this case, hydration only weakly shortens the decay time from 470 to 420 μs.

Chapter 5

Conclusions

This work focused on studying $AZrO_3$ (A=Ba, Sr or Ca) at varied doping concentration of yttrium. The study involved synthesis of the perovskite using a sol gel technique, and characterisation using XRD, IR spectroscopy and luminescence spectroscopy techniques.

Synthesis of the single-phase yttrium doped barium zirconate samples was possible up to 50%. At higher doping concentrations, splitting of the perovskite peaks was observed. Syntheses of 2.5% Y doped single-phase strontium and calcium zirconate samples were performed successfully.

Y doped $BaZrO_3$ samples were found to be cubic however increase of the Y concentration led to broadening of the peaks and shifting towards the lower 2θ angle. The 2.5% Y doped calcium zirconate and strontium zirconate systems were found to be orthorhombic structured.

The structure of the barium zirconate system became more and more distorted with increasing dopant concentration. There was a correlation between the Y dopant concentration and the local distortion of the perovskite structure. Doped samples with 20% yttrium deviated from the expected trends. These could be due to a possible transition from the cubic structure to a tetragonal as reported by Kreuer (2001) or ordering of the dopants in the perovskite structure. Changing the size of the A site atom had no effect on the Zr-O stretch of the perovskite.

From the studies of the dry and hydrated samples in the far infrared and mid infrared regions, the spectra for the hydrated and dry samples were similar indicating the presence of protons in the perovskite structure does not affect the vibrations of the A and B site ions. Luminescence spectroscopy identified an Eu site near lattice oxygen and a proton close to the dopant atom. This indicated both dopant atom-oxygen vacancy, and dopant atom proton-proton association effects in the material.

Outlook

Study in more detail the effect of the A site atom on the local structure of the perovskite and conductivity. This can be done by studying the vibrational behaviour using Raman and luminescence spectroscopy or changing the yttrium dopant concentration.

Study the symmetry around the dopant atom as a function of dopant concentration using luminescence spectroscopy. The luminescence spectroscopy was carried out only on 10% Yttrium doped samples. A study can be done for varying Yttrium concentrations in order to investigate the symmetry around the dopant atom with increasing concentration as well as any structural ordering in the 20% yttrium doped sample. This will help to understand the observed anomaly in the XRD and IR spectra during this study. Neutron diffraction could further be used to elucidate the structure of the 20% yttrium doped $BaZrO_3$

References

Alarcon J., Van Der Voort D., Blasse G. (1992). Efficient Eu^{3+} luminescence on non-lanthanide host lattices. Mat. Res. Bull., Vol. 27, pp. 467-472

Bi L., Fabbri E., Sun Z., Traversa E. (2011). Sinteractivity, proton conductivity and chemical stability of $BaZr_{0.7}In_{0.3}O_{3-\delta}$ for solid oxide fuel cells. Solid state Ionics, 196: 59-64

D'epifano A., Fabbri E., di Bartolommeo E., Licoccia S., Traversa E. (2007). Design of $BaZr_{0.8}Y_{0.2}O_{3-\delta}$ Protonic conductor to improve The Electrochemical Performance in Intermediate Temperature Solid Oxide Fuel Cells (IT-SOFCs) fuel cells 08, 2008, no. 1, 6976

Encyclopaedia of nations website.
http://www.nationsencyclopedia.com/Africa/Kenya-ENERGY-AND-POWER.html visited in September 2011

Fabbri E., Pergolesi D., Licoccia S., Traversa E. (2010). Does the increase in Y-dopant concentrations improve the proton conductivity of $BaZr_{0.8}Y_{0.2}O_{3-\delta}$ fuel cell electrolytes? Solid state Ionics, 181: 1043-1051

FTD (2001). Fuel cell today www.fuelcelltoday.com visited on September 12, 2011

Fuel cells (2011). www.fuelcell.org website visited on October 13, 2011

Garrison E. (2011). SOFC Solid Oxide fuel cells. Webpage visited ion September 2011

Glerup M, Poulsen F. W., Berg R W. (2002). Vibrational spectroscopy on protons

and deuterons in proton conducting perovskites. Solid state ionics, 148 83-92

IEA (2012). *World Energy Report*, International Energy Agency http://www.worldenergyoutlook.org/pressmedia/recentpresentations/presentationweo2012launch.pdf (IEA), presented in London

IEA (International Energy Agency), (2010). *World Energy Outlook 2010*, http://www.iea.org/publications/freepublications/publication/WEO2010_free.pdf Press release, 9 Nov 2010.

Iguchi F., Nagao Y., Sata N., Yugami H. (2011). Proton concentration in 15 mol % Y-doped $BaZrO_3$ proton conductors prepared at various temperatures. Solid state Ionics 192 97-100

Islam M. S., Davies R. A., Fisher C.A.J., Chadwick A. V. (2001). Defects and protons in the $CaZrO_3$, perovskites and $Ba_2In_2O_5$ brownmillerite: computer modelling and EXAFS studies. Solid state Ionics, 145: 333-338

Iwahara H. (1990). Protonic conduction in the single crystals of $SrZrO_3$ and $SrCeO_3$ doped with Y_2O_3 Solid state Ionics 40/41 910-913

Iwahara H., Esaka T., Uchida H., and Maeda N. (1981). Solid State Ionics 3-4, 359

Jenkins R. (1997). Quantitative X-ray Spectrometry Practical Spectroscopy; V. 20 New York: Marcel Decker

Johnson M., Lemmems P. (2005). Crystallography and Chemistry of Perovskites

Karlsson M., Ahmed I., Matic A., Eriksson S.G. (2010). Short-range structure of proton conducting $BaM_{0.10}Zr_{0.90}O_{2.95}$ (M= Y, In, Sc and Ga) investigated with vibrational spectroscopy. Solid state Ionics, 181: 126-129

Karlsson M., Matic A., Knee C. S., Ahmed I., Eriksson S.G., Borjesson L. (2007). Short range structure of proton conducting perovskite $BaIn_xZr_{1-x}O_{3-x/2}$ (x = 0 – 0.75)

Karlsson M., Bjrketun M. E., Sundell P. G., Matic A., Wahnstrm G., Engberg D., Brjeson L. (2005). Vibrational properties of protons in hydrated $BaIn_xZr_{1-x}O_{3-\delta}$. Physical Review B72, 094303 1098-0121

Kreuer K. D. (1999). Aspects of the formation and mobility of protonic charge carriers and the stability of perovskite type oxides. Solid state Ionics 125 285-302

Kreuer K.D. (2000). On the complexity of proton conduction phenomena. Solid state Ionics 137-137 149-160

Kreuer K.D. (2003). Proton-Conducting oxides. Annu. Rev. Mater. Res. 33333-59

Kreuer K. D., Adams St., Munch W., Fuchs A., Klock U., Maier J. (2001). Proton conducting alkaline earth zirconates and titanates for high drain electro-chemical applications. Solid state Ionics, 145: 295-306

KV30 (2010) Kenya Vision 2030, Popular version from Kenya Vision 2030 website: http://www.vision2030.go.ke/cms/vds/Popular_Version.pdf

Larkin P. J. (2011). *IR and Raman spectroscopy: Principles and Spectral interpretation.* USA: Elsevier

Last J. T. (1957). Infrared-Absorption Studies on Barium Titanate and Related Materials. Physical review 105(6) 1740-1750

Malavasi L., Fisher C. A. J., M. Saiful Islam (2010). Oxide-ion and proton conducting electrolyte materials for clean energy applications: structural and mechanistic features. Chemical Society Reviews. DOI: 10.1039/b915141a

Munch W., Kreuer K. D., Seifert G., Maier J. (2000). Proton diffusion in perovskites: comparison between $BaCeO_3$, $BaZrO_3$, $SrTiO_3$ and $CaTiO_3$ using quantum molecular dynamics. Solid state Ionics, vol 136-137, pg183-189

Münch W., Seifert G., Kreuer K. D., and Maier J. (1996). Solid State ionics 86-88, 647□.

NEP (2004). (National Energy Policy), sessional paper no 4 of 2004. http://www.energy.go.ke/downloads/SESSIONAL%20PAPER%204%20ON%20ENERGY%202004.pdf Retrieved on September 11, 2011.

Nakagawa I., Tuschida A., Shimanochi T., (1967). Infrared Transmission Spectrum and Lattice Vibration Analysis of Some Perovskite Fluorides. The journal of chemical physics. 47 982-989

Norby Truls (1999). Solid-state protonic conductors: Principles, properties, progress and prospects. Solid state Ionics 125 1-11

Norby Truls (2001). The promise of protonics. Nature 410 877-878

Omata T., Takagi M., Matsuo S. Y. O. (2004). O-H stretching vibrations of proton conducting alkaline-earth zirconates. Solid state Ionics 168, 99-109

Ormerod R. M. (2003). Solid Oxide Fuel cells. Chemical Society review 32, 17-28

PDX (2011). XRD basics PDX http://web.pdx.edu/~pmoeck/phy381/Topic5a-XRD.pdf visited on 12 September 2011

Perry C. H., McCarthy D. J., Rupprecht G. (1965). Dielectric dispersion of some perovskite zirconates. Physical review, 138, 5A

Sata N., Sone H., Kitamura N., Hattori T., Ishigame M. (2000). O-H Stretching vibration in a perovskite-type proton conducting super lattice. Solid state Ionics, vol 136-137, pg. 197-201

Settle A. F. (1997). *Handbook of Instrumental Techniques for Analytical Chemistry*. New Jersey: Prentice Hall

Shannon, R.D. (1976). Revised Effective Ionic Radii and Systematic Studies of Interatomic Distances in Halides and Chaleogenides. Acta Cryst. . A32, 751

Steele B. C. H., Heinzel A. (2001). Materials for fuel cell technologies. Nature, 414: 345-352

Tsuji K. Injuk J. Grieken R. (2004). X-Ray Spectrometry: Recent Technological Advances Wiley and sons

UNR (1998). Schmitt C. G., MS thesis

WB (World Bank) (2012). *Energy Report 2012*. World bank website visited on 5th February 2013.

Wartewig S. (2003). *IR and Raman Spectroscopy: Fundamental Processing.* Germany: Wiley vch

WES *(World Energy Statistics*) (2012). http://alofatuvalu.tv/FR/12_liens/12_articles_rapports/IEA_rpt_2012_us.pdf

International Energy Agency visited in June 2012

Wikipedia (2011). Infrared spectroscopy http://en.wikipedia.org/wiki/Infrared_spectroscopy visited on 15th September 2011

Wikipedia (2011). Bragg law. http://en.wikipedia.org/wiki/Bragg's_law visited on December 31 2011

Wikipedia (2012). https://en.wikipedia.org/wiki/Goldschmidt_tolerance_factor page visited June 2012

Yajima T., Suzuki H. Yogo T., Iwahara H. (1992). Protonic conduction in $SrZrO_3$-based oxides. Solid state Ionics, 51: 101-107

Appendix A

Infrared

The figure below shows the spectra for the hydrated $BaZr_{1-x}Y_xO_{3-x/2}$ samples in the far infrared (FIR) and mid infrared (MIR) regions. Comparing these results with the dry spectra in the results, it can be observed that the peak positions remain unchanged for both the dry and hydrated spectra. They differ in the sharpness of the peaks. The dry spectra were more defined than those of the hydrated samples.

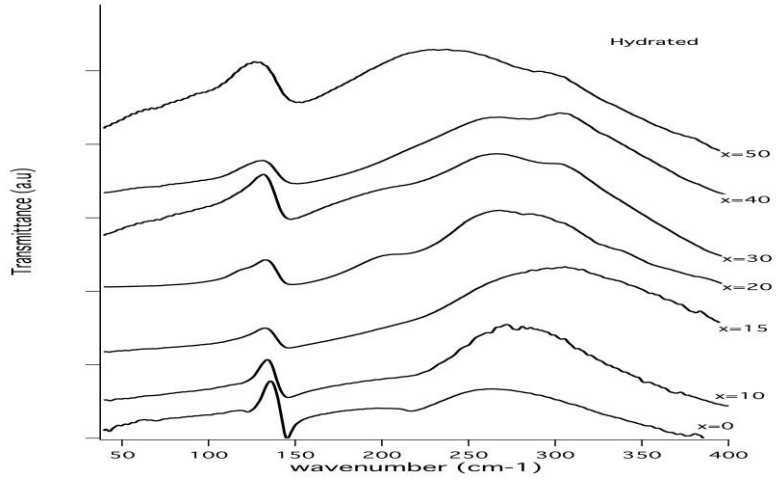

Figure: A-1 FIR spectra for the hydrated $BaZr_{1-x}Y_xO_{3-x/2}$ samples with absorption bands observed at 140 cm^{-1}, 280 cm^{-1} and 330 cm^{-1}. The spectra have been vertically offset for clarity

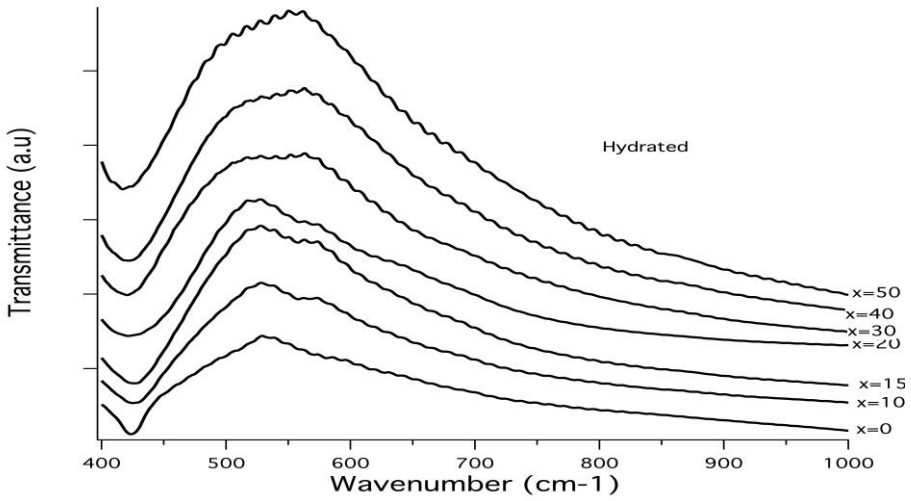

Figure A-2: MIR spectra for the hydrated $BaZr_{1-x}Y_xO_{3-x/2}$ samples with absorption bands observed at 550 cm^{-1} and 570 cm^{-1}. The spectra have been vertically offset for clarity

The figure below shows the spectra for the dry sample in the O-H stretch region. A weak band (compared to that of the hydrated sample) is observed. This is due to the fact that it is difficult to remove all protons from the sample. (Karlsson et al., 2005). Of note though is the absence of the vibrational band observed at 4250 cm^{-1} in the hydrated sample.

Fit parameters for the spectra in the O-H region and the fitted spectra

Table A-1: Table showing the fit parameters for the four Gaussian bands according to equation 4.1 for $BaZr_{1-x}Y_xO_{3-x/2}$ samples. i=1,2, 3,4

$x/band$	$a_i * 10^{2}$	$b_i(2d.p)$	$x_i(1d.p)$
10 1	7.590 ± 0.39	75.50 ± 8.14	2725.6 ± 16.600
2	22.460 ± 4.93	328.83 ± 3.71	3113.0 ± 6.300
3	25.350 ± 5.37	203.60 ± 2.06	3378.8 ± 0.551
4	12.760 ± 1.70	97.755 ± 0.60	3568.4 ± 0.252
15 1	10.090 ± 5.00	438.52 ± 10.50	2754.0 ± 20.80
2	23.443 ± 9.98	315.89 ± 6.37	3122.4 ± 4.970
3	24.548 ± 7.88	195.73 ± 2.76	3383.1 ± 0.576
4	14.068 ± 2.11	91.47 ± 0.65	3563.8 ± 0.263
20 1	6.058 ± 0.81	451.69 ± 23.70	2771.2 ± 52.700
2	14.057 ± 1.49	314.58 ± 13.90	3103.7 ± 5.990
3	16.279 ± 7.33	192.57 ± 3.25	3372.6 ± 0.664
4	8.726 ± 1.43	89.478 ± 0.711	3555.0 ± 0.294
30 1	9.898 ± 3.85	477.12 ± 13.70	2674.3 ± 22.100
2	27.362 ± 9.49	323.36 ± 6.39	3109.8 ± 4.410
3	23.836 ± 8.38	194.79 ± 3.16	3383.5 ± 0.690
4	13.997 ± 2.37	87.621 ± 0.77	3560.9 ± 0.282
40 1	17.094 ± 1.52	465.06 ± 16.60	2856.0 ± 36.900
2	28.145 ± 3.20	302.56 ± 16.60	3177.6 ± 10.700
3	23.519 ± 0.69	93.67 ± 0.97	3569.9 ± 0.316
4	27.183 ± 2.22	179.03 ± 6.01	3418.8 ± 1.850
50 1	25.025 ± 0.52	393.99 ± 4.75	2987.6 ± 8.780
2	27.313 ± 1.31	246.86 ± 5.95	3284.9 ± 4.230
3	22.697 ± 1.15	142.60 ± 3.18	3470.0 ± 1.760
4	20.251 ± 0.53	78.821 ± 0.63	3576.3 ± 0.148

Appendix B

How a fuel cell works: Theoretical background

The purpose of a fuel cell is to produce an electrical current that can be directed outside the cell to do work, such as powering an electric motor or illuminating a light bulb or a city. Because of the way electricity behaves, this current returns to the fuel cell, completing an electrical circuit. Hydrogen atoms enter a fuel cell at the anode where a chemical reaction strips them of their electrons. The hydrogen atoms are now ionized, and carry a positive electrical charge. The negatively charged electrons provide the current through wires to do work. If alternating current (AC) is needed, the DC output of the fuel cell must be routed through a conversion device called an inverter. Oxygen enters the fuel cell at the cathode; it therefore combines with electrons returning from the electrical circuit and hydrogen ions that have travelled through the electrolyte from the anode. (Garrison, 2011)

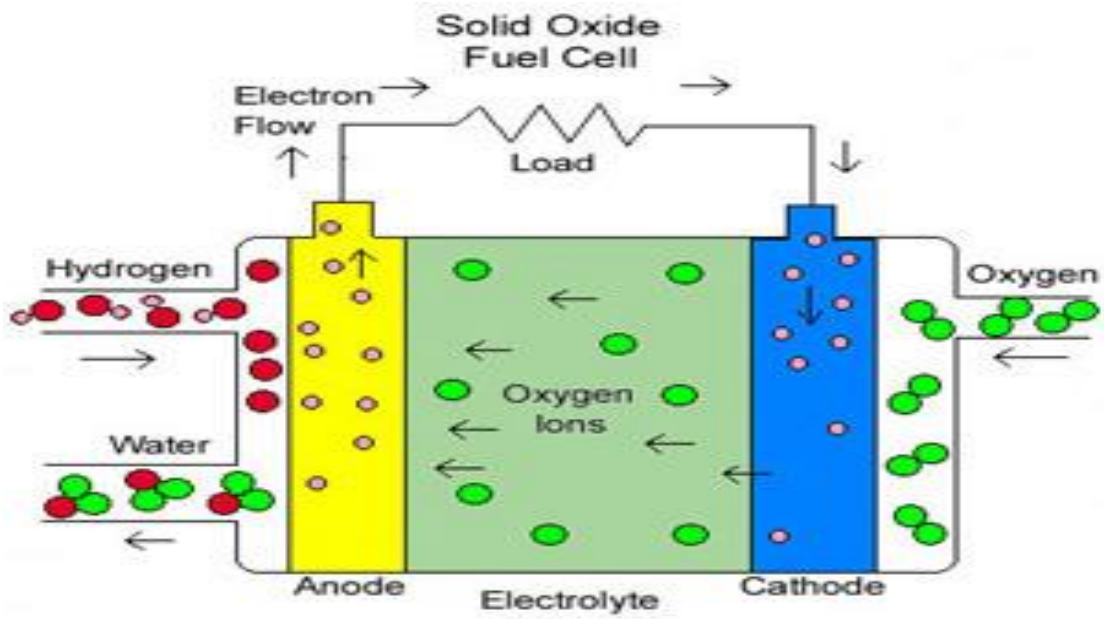

Figure B-1: (SOFC). The SOFC is simpler, more efficient than any other fuel cell variant (Steele, 2001).

The electrolyte plays a key role. It must permit only the appropriate ions to pass

between the anode and cathode. If free electrons or other substances could travel through the electrolyte, they would disrupt the chemical reaction. Oxygen and hydrogen combine to form water As long as a fuel cell is supplied with hydrogen and oxygen, it will generate electricity.

Types of fuel cells

A range of different fuel cells exists. Examples include Alkaline Fuel Cell (AFC), Polymeric- Electrolyte Membrane Fuel Cell (PEMFC), Phosphoric Acid Fuel Cell (PAFC), Molten Carbonate Fuel Cell (MCFC) and the Solid Oxide Fuel Cells. The fuel cells may be divided into different categories depending on the nature of the electrolyte, which is the heart of a fuel cell. A good electrolyte material has a sufficiently high ionic conductivity, negligible electronic conductivity, stable in both reducing and oxidising atmospheres, chemical stability and mechanical strength. (Garrison, 2011)

Polymer Electrolyte Fuel Cell (PEFC)

The electrolyte in this fuel cell is an ion exchange membrane (fluorinated sulfonic acid polymer or other similar polymer) that is an excellent proton conductor. The only liquid in this fuel cell is water; thus, corrosion problems are minimal. Typically, carbon electrodes with platinum electro- catalyst are used for both anode and cathode, and with either carbon or metal interconnects. Water management in the membrane is critical for efficient performance; the fuel cell must operate under conditions where the by-product water does not evaporate faster than it is produced because the membrane must be hydrated. Because of the limitation on the operating temperature imposed by the polymer, usually less than 100 ˚C, but more typically around 60 to 80 ˚C, and because of problems with water balance, a H_2-rich gas with minimal or no CO (a poison at low temperature) is used. Higher catalyst loading (Pt in most cases) than that used in PAFCs is required for both the anode and cathode. Extensive fuel processing is required with other fuels, as even trace levels of CO, sulphur species, and halogens easily poison the anode. (Garrison, 2011)

Alkaline Fuel Cell (AFC)

The electrolyte in this fuel cell is concentrated (85 wt per cent) KO-H in fuel cells operated at high temperature (250 ˚C), or less concentrated (35 to 50 wt per cent) KO-H for lower temperature (<120 ˚C) operation. The electrolyte is retained in a matrix (usually asbestos), and a wide range of electro-catalysts can be used (e.g., Ni, Ag, metal oxides, spinels, and noble metals). The fuel supply is limited to non-reactive constituents except for hydrogen. CO is a poison, and CO_2 will react with the KO-H to form K_2CO_3, thus altering the electrolyte. Even the small amount of CO_2 in air must be considered a potential poison for the alkaline cell. Generally, hydrogen is considered as the preferred fuel for AFC, although some direct carbon fuel cells use (different) alkaline electrolytes. (Garrison, 2011)

Phosphoric Acid Fuel Cell (PAFC)

Phosphoric acid, concentrated to 100%, is used as the electrolyte in this fuel cell, which typically operates at 150 to 220 ˚C. At lower temperatures, phosphoric acid is a poor ionic conductor, and CO poisoning of the Pt electro-catalyst in the anode becomes severe. The relative stability of concentrated phosphoric acid is high compared to other common acids; consequently the PAFC is capable of operating at the high end of the acid temperature range (100 to 220 ˚C). In addition, the use of concentrated acid (100%) minimizes the water vapour pressure so water management in the cell is not difficult. The matrix most commonly used to retain the acid is silicon carbide (1), and the electro-catalyst in both the anode and cathode is Pt. (Garrison, 2011)

Molten Carbonate Fuel Cell (MCFC)

The electrolyte in this fuel cell is usually a combination of alkali carbonates, which is retained in a ceramic matrix of $LiAlO_2$. The fuel cell operates at 600 to 700 ˚C where the alkali carbonates form a highly conductive molten salt, with carbonate ions

providing ionic conduction. At the high operating temperatures in MCFCs, Ni (anode) and nickel oxide (cathode) are adequate to promote reaction. Noble metals are not required for operation, and many common hydrocarbon fuels can be reformed internally. (Garrison, 2011)

Luminescence spectroscopy

Luminescence is the emission of light by a substance. It occurs when an electron returns to the electronic ground state from an excited state and loses it's excess energy as a photon. At the lowest excited singlet state, the molecule may be completely deactivated by the solvent (quenching), may fluoresce. The observed fluorescence will show two important characteristics:

1. Fluorescence may appear as an approximate mirror image of the absorption at a lower energy, and hence lower frequency (longer wavelength) than the absorption, the difference (in wavenumbers) between the two corresponding bands being known as the Stokes shift.

2. Fluorescence emission may show vibrational structure, which can provide information about the force constants of the molecule in its ground state (the electronic structure provides information about the force constants in the excited state). Time of radiation = time of fluorescence.

O-H has a vibrational frequency of about 3500^{-1} which can result in quenching of an excited sample.